AGU PUBLICATIONS

JGR

Journal of Geophysical Research: Solid Earth

RESEARCH ARTICLE
10.1002/2017JB014121

This article is a companion to *Massiot et al.* [2017] doi:10.1002/2017JB014115.

Key Points:
- Fracture spacing is predominantly lognormal and controlled by lava flow stratification, with subordinate fault-controlled power law spacing
- Thickness is controlled by isotropic (thermal) factors in thin section, and by anisotropic (tectonic) factors at core and BHTV log scales
- Approximately 5% of the rock mass is occupied by fractures at thin-section, core, and BHTV log scales

Supporting Information:
- Supporting Information S1
- Table S1
- Table S2
- Table S3
- Table S4
- Figure S1

Correspondence to:
C. Massiot,
c.massiot@gns.cri.nz

Citation:
Massiot, C., A. Nicol, D. D. McNamara, and J. Townend (2017), Evidence for tectonic, lithologic, and thermal controls on fracture system geometries in an andesitic high-temperature geothermal field, *J. Geophys. Res. Solid Earth*, *122*, 6853–6874, doi:10.1002/2017JB014121.

Received 20 FEB 2017
Accepted 21 JUL 2017
Published online 26 AUG 2017

Evidence for tectonic, lithologic, and thermal controls on fracture system geometries in an andesitic high-temperature geothermal field

Cécile Massiot[1,2], Andrew Nicol[3], David D. McNamara[2,4], and John Townend[1]

[1]School of Geography, Environment, and Earth Sciences, Victoria University of Wellington, Wellington, New Zealand, [2]GNS Science, Lower Hutt, New Zealand, [3]Department of Geological Sciences, University of Canterbury, Christchurch, New Zealand, [4]Earth and Ocean Sciences, School of Natural Sciences, National University of Ireland, Galway, Ireland

Abstract Analysis of fracture orientation, spacing, and thickness from acoustic borehole televiewer (BHTV) logs and cores in the andesite-hosted Rotokawa geothermal reservoir (New Zealand) highlights potential controls on the geometry of the fracture system. Cluster analysis of fracture orientations indicates four fracture sets. Probability distributions of fracture spacing and thickness measured on BHTV logs are estimated for each fracture set, using maximum likelihood estimations applied to truncated size distributions to account for sampling bias. Fracture spacing is dominantly lognormal, though two subordinate fracture sets have a power law spacing. This difference in spacing distributions may reflect the influence of the andesitic sequence stratification (lognormal) and tectonic faults (power law). Fracture thicknesses of 9–30 mm observed in BHTV logs, and 1–3 mm in cores, are interpreted to follow a power law. Fractures in thin sections (~5 μm thick) do not fit this power law distribution, which, together with their orientation, reflect a change of controls on fracture thickness from uniform (such as thermal) controls at thin section scale to anisotropic (tectonic) at core and BHTV scales of observation. However, the ~5% volumetric percentage of fractures within the rock at all three scales suggests a self-similar behavior in 3-D. Power law thickness distributions potentially associated with power law fluid flow rates, and increased connectivity where fracture sets intersect, may cause the large permeability variations that occur at hundred meter scales in the reservoir. The described fracture geometries can be incorporated into fracture and flow models to explore the roles of fracture connectivity, stress, and mineral precipitation/dissolution on permeability in such andesite-hosted geothermal systems.

Plain Language Summary High-temperature geothermal systems provide reliable and sustainable renewable energy. In systems hosted in volcanic rocks, fluid flow necessary to generate electricity dominantly circulates through fractures, which remain difficult to target before expensive drilling. Analysis of fractures measured in underground boreholes of the Rotokawa Geothermal Field (New Zealand) highlights the role of the original rock formations (a sequence of lava flows), tectonic forces (faults), and cooling controls on the fracture system. Faulting and cooling controls were known, but the effects of the original layering of the lava flows had not previously been identified. The density of fractures in the rock evaluated at different scales of observation can be used to generate predictive models of fracture distributions in the geothermal reservoir, and to further advance knowledge on the evolution of fracture systems through a complex history of volcanism, hydrothermal circulations and faulting. Geothermal systems hosted in volcanic rocks have been in operation in, e.g., New Zealand and Indonesia, and are in exploration in Chile and other countries, with great potential but very limited available data. Results from the Rotokawa Geothermal Field will thus help with the understanding and development of geothermal fields in New Zealand and worldwide.

1. Introduction

Non sedimentary rocks are increasingly recognized as reservoirs able to produce fluids. Volcanic formations host geothermal [*Arnórsson*, 1995; *Nemčok et al.*, 2004; *Wilson and Rowland*, 2016], groundwater [*Lachassagne et al.*, 2014], hydrocarbon [*Feng*, 2008], and mineral [*Spörli and Cargill*, 2011] resources, while also being capable of storing unwanted CO_2 [*Pollyea et al.*, 2014; *Matter et al.*, 2016] and radioactive waste [*Chen et al.*, 2001], and capable of supporting surface engineering projects [*Alemdag*, 2015]. The geometry of vesicles

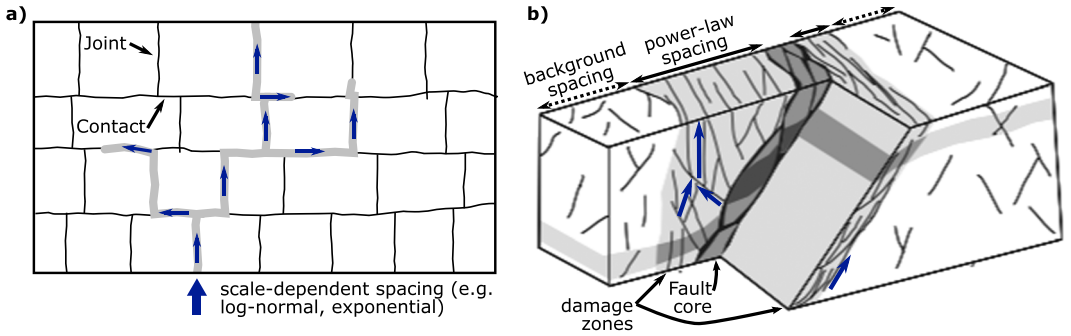

Figure 1. Schematic fracture and fluid flow models. (a) In layered jointed rocks, flow can occur along joints and contacts between layers; the layer thickness and ratio of layer tensile to interface shear strength [*Schöpfer et al.*, 2011] are characteristic scales that affect the joint spacing [after *Gudmundsson et al.*, 2002]. (b) In fault damage zones, fracture spacing is clustered near faults (commonly power law), and a background spacing (power law or scale dependent) prevails away from the fault zone [after *Manzocchi et al.*, 2010].

and fractures in volcanic units has been extensively studied in outcrops [e.g., *DeGraff and Aydin*, 1987; *Gudmundsson*, 2000; *Conway et al.*, 2015] but can be difficult to quantify in reservoirs due to sparse core and wireline logging measurements. In lava-hosted reservoirs, permeability is strongly influenced by faults and fractures [e.g., *Nemčok et al.*, 2007; *Davatzes and Hickman*, 2010; *McNamara et al.*, 2015], but the key fracture attributes are often not sufficiently well constrained to make accurate fluid flow predictions [*Aprilina et al.*, 2015; *Hernandez et al.*, 2015; *Kissling et al.*, 2015].

Description of the three-dimensional (3-D) geometry of a fracture system is necessary to develop reservoir-scale models which can assist resource management [*Bonnet et al.*, 2001; *Berkowitz*, 2002; *Chilès*, 2005] and constrain the origin and evolution of the fracture systems [*Ackermann et al.*, 2001; *McCaffrey et al.*, 2003]. Fracture systems can be described in terms of the orientation of different fracture sets, and the probability distribution of fracture attributes: aperture (for open fractures), thickness (for veins), spacing, density, and length [*Priest*, 1993]. The probability distribution of fracture attributes varies as a function of the processes that control fracture generation and propagation [*Bonnet et al.*, 2001; *André-Mayer and Sausse*, 2007]. In layered systems, joint spacing is usually best approximated by scale-dependent distributions (such as regular, lognormal, gamma, or exponential), with characteristic sizes linked to the layer thickness and ratio of the layer tensile to interface shear strength [*Rives et al.*, 1992; *Gillespie et al.*, 1993; *Schöpfer et al.*, 2011]. Fluids tend to flow along these joints and contacts between layers (Figure 1a). In contrast, the spacing of fractures close to faults are commonly clustered according to power law distributions which are scale independent (Figure 1b) [see *Bonnet et al.*, 2001, for review; *McCaffrey et al.*, 2003; *Johri et al.*, 2014]. Power law distributions of fracture mechanical aperture, length, and density are commonly used to generate reservoir-scale fracture models [*Bonnet et al.*, 2001; *Davy et al.*, 2013], albeit resulting from observations rarely made in volcanic formations.

In reservoirs, the scaling of fracture attributes is typically evaluated using sparse cores and borehole image logs such as acoustic borehole televiewer (BHTV) logs, which provide an oriented image of the inside of a borehole [*Hansen and Buczak*, 2010]. Image logs have been acquired in high temperature (>250°C) geothermal fields of the Taupo Volcanic Zone (TVZ; New Zealand) since 2009 and provided the first direct observations of structures in the reservoirs [*McNamara and Massiot*, 2016, and references therein]. To date, little work has been conducted on the fracture geometries and densities in these systems, and on the factors that control the fracture system architecture. The Rotokawa reservoir, TVZ, is a high-temperature faulted reservoir hosted in andesitic lavas and breccias [*McNamara et al.*, 2016a, and references therein], where fractures are thought to be the major control on the flow of hot fluids [*McNamara et al.*, 2015]. The available BHTV logs, as well as cores and thin sections collected during the past 50 years, provide a rare opportunity to evaluate the fracture system organization in a hydrothermally altered, 1 km thick sequence of lava flows.

In this study, we statistically analyze fracture orientation, thickness, spacing, and volumetric densities at BHTV log scale, complemented by core observations and previously reported measurements on thin sections, from the Rotokawa Geothermal Field. We address three major questions: (1) Is the fracture spacing scale independent, hence suggesting a fault control on fracture locations, or scale dependent, suggesting a control

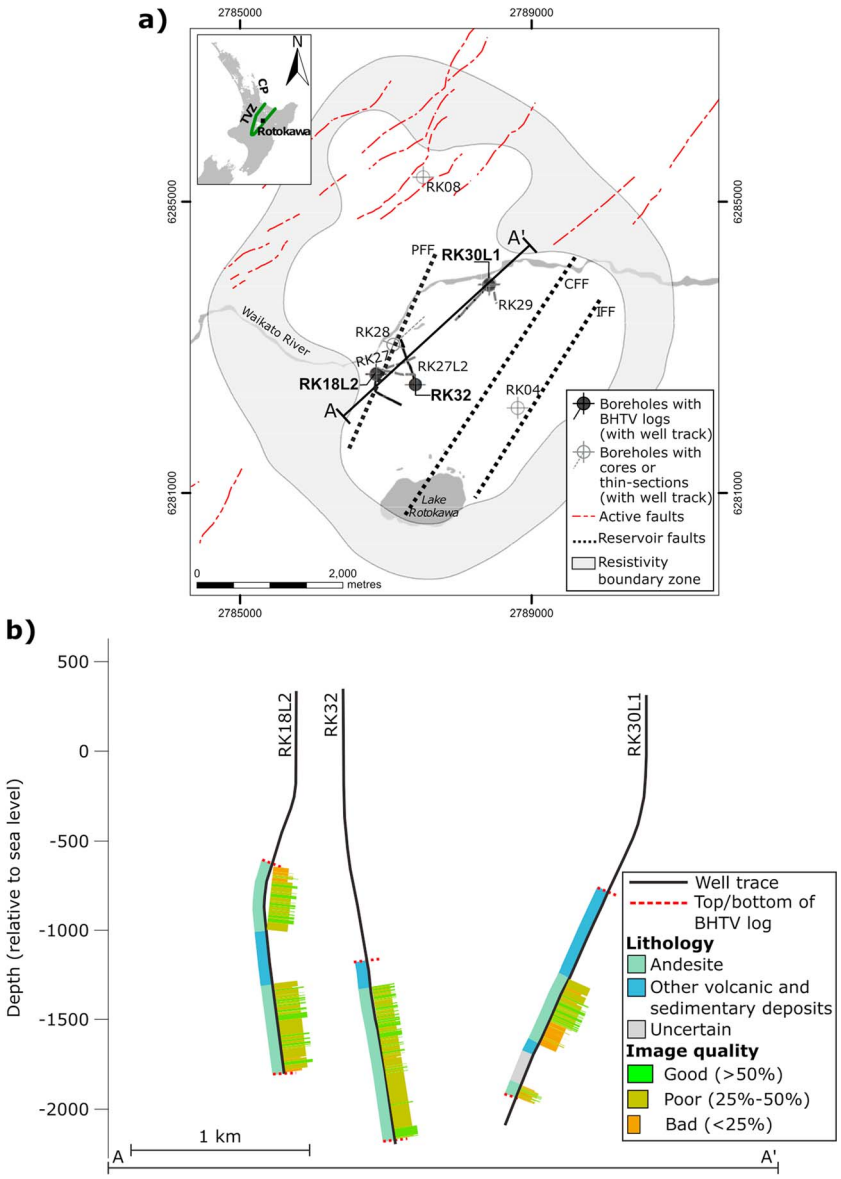

Figure 2. (a) Location map of the Rotokawa Geothermal Field including the approximate resistivity boundary zone at about 500 m depth [after *Risk*, 2000], the mapped active faults (GNS Science active fault database, http://data.gns.cri.nz/af/) [*Litchfield et al.*, 2014], the inferred faults projected from the top of the Rotokawa Andesite [*Wallis et al.*, 2013], and the location of the boreholes where the cores, thin sections, and three BHTV logs used in this study have been collected. PFF: principal field fault; CFF: central field fault; IFF: injection field fault. Insert displays the location of the Rotokawa Geothermal Field, Taupo Volcanic Zone (TVZ), and the Coromandel Peninsula (CP). (b) Cross section (Line A-A' in Figure 2a) with projected RK18L2, RK30L1, and RK32 borehole tracks (surface topography is subplanar). Left side of well traces colored for lithology (determined from drill cuttings/core and geological modeling) and right side colored for BHTV log quality (total percentage of good azimuthal coverage).

by the layered host lithology?; (2) Is there a continuous relationship between fracture thickness at the three scales of observation (thin section, core, and BHTV log)?; and (3) What is the overall fracture density? The resulting concepts and measurements have wide applications for improving our understanding of how fracture systems develop in andesite-hosted geothermal reservoirs, which will produce better fluid flow models for improved resource management.

2. Geological Settings

The Rotokawa Geothermal Field is located ~10 km north of Taupo, New Zealand, on the eastern side of the Taupo Volcanic Zone (TVZ; Figure 2a). The TVZ is the active, southern portion of the Lau-Havre-Taupo

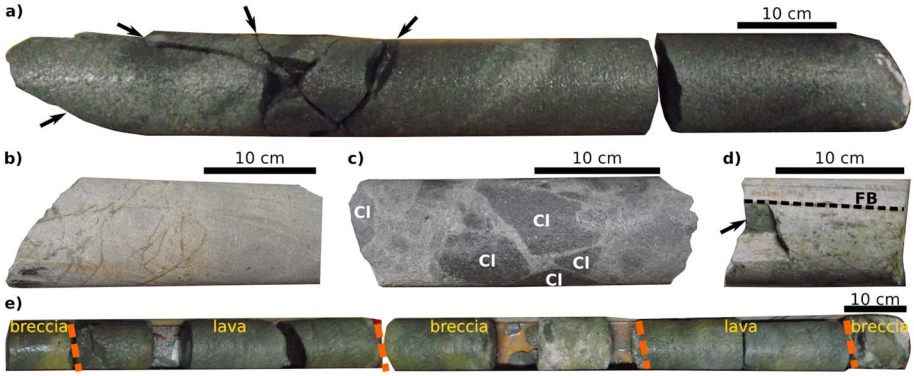

Figure 3. Lithologies, alteration, and fracturation observed in cores from the Rotokawa Geothermal Field. (a) Moderately altered andesite lava with low fracture density (arrows indicate natural fractures); RK27L2 #1. (b) Strongly altered andesite lava with high (on the left) to low (on the right) epidote-filled fracture density; RK29 #1. (c) Moderately altered andesite breccia with large clasts ("Cl") and low fracture density. Thin white calcite and quartz veins surround the clasts; RK27 #1. (d) Flow-banded rhyolite lava with fracture (arrow) aligned with flow-banding ("FB"); RK4 #3. (e) Intercalation of andesite lava and breccia (dashed lines between lithology changes). The core names refer to Table 1.

extensional intra-arc basin, which formed as a result of the oblique subduction of the Pacific plate beneath the Australian plate [*Begg and Mouslopoulou*, 2010; *Rowland and Simmons*, 2012; *Wilson and Rowland*, 2016]. The TVZ is ~350 km long and up to ~60 km wide, extending from the Ruapehu volcano to the Bay of Plenty and beyond to White Island [*Wilson et al.*, 1995]. Clockwise vertical axis rotation of the eastern North Island has accompanied the formation of NE-SW striking normal faults defining the Taupo Rift, resulting in a contemporary NW-SE directed extension rate of the order of 1 cm/yr [*Wallace et al.*, 2004; *Nicol et al.*, 2006]. These normal faults are laterally discontinuous and typically dip 60–80° at the ground surface [*Rowland and Sibson*, 2001; *Villamor and Berryman*, 2001, 2006; *Rowland et al.*, 2010; *Seebeck et al.*, 2010].

Rotokawa is an operating geothermal field with a total installed electricity production capacity of 174 MW [*Hernandez et al.*, 2015]. The geology of the field comprises volcano-sedimentary and andesitic formations ≤1.9 Ma [*Chambefort et al.*, 2014], which overlie older faulted Rotokawa Andesite units and the Mesozoic Greywacke basement [*McNamara et al.*, 2016a]. The Rotokawa Andesite is an 800–2100 m thick unit of andesite lavas and breccias and is inferred to form a large buried andesitic volcano which is also partly located under the nearby Ngatamariki Geothermal field [*Browne et al.*, 1992; *Chambefort et al.*, 2014]. The deep, hot (320°C) aquifer is hosted in these low matrix porosity (4–15%) andesites [*Siratovich et al.*, 2014; *Hernandez et al.*, 2015], in which fluid flow is mostly controlled by fractures and faults [*McNamara et al.*, 2015]. Three large (0–400 m throw) NE-SW striking normal faults have been inferred within the geothermal field based on stratigraphy defined from 35 boreholes, reservoir temperatures, and microseismicity (Figure 2a) [*Wallis et al.*, 2013; *Sherburn et al.*, 2015]. The faults generate offsets observed in the Greywacke basement and Rotokawa andesites but are thought not to propagate into the overlying units where stratigraphic offsets between wells are not observed. These faults are consistent with a normal faulting regime [*Davidson et al.*, 2012] and an azimuth of maximum horizontal compression stress (S_{Hmax}) oriented approximately NE-SW, although variations in S_{Hmax} occur between and within wells [*McNamara et al.*, 2015]. The reservoir has a heterogeneous permeability distribution, for example, with one of the three main faults inferred to form a barrier to flow [*Hernandez et al.*, 2015; *Sherburn et al.*, 2015]. Current stratigraphic information in these hydrothermally altered andesites precludes lateral facies correlation across the field.

3. Data

Statistical analysis of the fracture system hosted in Rotokawa andesitic formations is primarily performed here on fractures interpreted from the BHTV logs, which provide near-continuous 1-D sampling lines. Spot core fracture analyses (presented here for the first time) give details on the rock types and extend the scale of thickness and density observations made on BHTV logs. Previously reported thin-section data further inform fracture thicknesses and densities at subcore scales [*Siratovich et al.*, 2014].

3.1. Core

Cores in the Rotokawa Geothermal Field display a variety in their fracture attributes (density, orientation, and infilling minerals), volcanic lithologies, and hydrothermal alteration (Figure 3). Volcanic rocks sampled by

Table 1. Lithology, Alteration Intensity, Measured Depth of Studied BHTV Log and Cores, and Fracture Abundance (See Section 4.3 for Explanations of P_{10}, P_{32}, and P_{33}) Measured in BHTV Logs, Cores, and Thin Section[a]

					n		P_{10} (m^{-1})		P_{32} (m^{-1})		P_{33} (vol %)	
Borehole	Lithology	Alteration	Depth (m)	Length (m)	*r*	*c*	*r*	*c*	*r*	*c*	*r*	*c*
RK18L2 (b)	A		995–1,385	844.7	324	1,255.9	0.4	1.5	0.9	4.3	0.7	3.1
RK30L1 (b)	A		$\frac{1,710-2,255}{1,660-2,060}$	307.1	276	835	0.9	2.7	2.4	8.4	2.3	8.7
RK32 (b)	A		$\frac{2,320-2,405.5}{1,712-2,639}$	921.8	533	1,410.5	0.6	1.5	1.4	4.6	1.9	6.4
Mean (b)	A			2,073.5	1,133	3,501.4	0.5	1.7	1.4	5	1.5	5.4
RK04 #3 (c)	Rl	strong	700–702	0.74	20	71.7	27	96.9	31	114	3.4	15.9
RK08 #5 (c)	tuff	strong	1,412–1,414	1.13	6	11.8	5.3	10.4	8.7	17.3	1	1.9
RK08 #7 (c)	Al	weak	1,953–1,955	0.58	7	39.8	12.1	68.7	17.9	115.8	1.8	11.6
RK08 #7 (c)	Ab	moderate	1,953–1,955	0.54	2	7.3	3.7	13.5	4.4	16.1	0.5	1.3
RK08 #8 (c)	Al	moderate	2,219–2,227	0.41	12	53	29.3	129.4	34.1	138.6	6.4	27
RK08 #8 (c)	Al	strong	2,219–2,227	1.28	32	182.7	25	142.7	32.9	207.6	3.8	23.9
RK27 #1 (c)	Ab	strong	1,850–1,856	2.44	5	19.7	2	8.1	1.7	6.4	0.3	1.2
RK27 #2 (c)	Al	weak	2,147–2,153	2.83	29	102.9	10.2	36.4	15.6	60.4	1.9	7.9
RK27 #2 (c)	Al	moderate	2,147–2,153	0.74	0	0	0	0	0	0	0	0
RK27 #2 (c)	Ab	moderate	2,147–2,153	1.12	8	33.4	7.1	29.8	10	42.1	1.3	5
RK27L2 #1 (c)	Al	moderate	2,120–2,126	2.44	21	51.3	8.6	21	12	31.6	0.8	1.9
RK29 #1 (c)	Al	strong	2,081.4–2,084.4	1.69	45	117.2	26.6	69.3	25.5	79.9	3	8.8
RK30L1 #1 (c)	tuff	strong	11,13.6–11,20.2	6.6	0	0	0	0	0	0	0	0
Mean (c)	A			14.81	181	679.1	12.2	45.8	14.8	59.1	1.7	7
Mean (c)	all			22.55	187	690.9	8.3	30.6	7.6	29.5	0.9	3.5
RK27L2; RK28; RK30L1 (ts)	A							1,830–15,530[b]		3,770–13,060[b]		1.9–6.5[b]
Mean (ts)	A							4721[b]		8103[b]		4.0[b]

[a]Presented thin section data contains the range (minimum-maximum) and mean values measured in the 10 thin sections analyzed in *Siratovich et al.* [2014]. P_{33} for thin sections was calculated from the P_{32} and a mean fracture thickness of 5 μm. The length of log correspond to length of moderate quality (>25% borehole coverage) used in the analysis. (b): BHTV logs; (c): core; (ts): thin section; #: core number within each borehole; A: undifferentiated andesite lava and breccia; Al: andesite lava; Ab: andesite breccia; Rl: rhyolite lava; tuff: tuff of the Wairakei Ignimbrite; all: mean for all cores; r: raw measurements; c: measurements corrected for orientation bias.

[b]Thin section measurements were not corrected for orientation bias, but fracture orientation is isotropic and therefore comparable to corrected measurements in cores and BHTV logs.

the cores have been subject to pervasive alteration consisting of a propylitic-style hydrothermal assemblage (quartz, wairakite, epidote, clinozoisite, illite, chlorite, adularia, albite, and calcite), with an intensity varying from weak to strong [*McNamara et al.*, 2016a, and references therein]. Average clast size of breccias (Figure 3c) is 26 ± 22 mm (one standard deviation). Although most cores comprise only one lithology (Table 1), alteration intensity can vary at decimeter scale, and both andesite lava and breccia can occur over tens of centimeters (Figure 3e).

In this study, 181 natural fractures were described in 14.8 m cumulative length of core in four boreholes which penetrated andesite lavas, rhyolite lava (Haparangi rhyolite), and andesite breccias (Table 1). In addition, six fractures were measured from cores of partially welded to welded tuff of the Wairakei Ignimbrite in two further boreholes. Forty-nine other cores collected from the Rotokawa Geothermal Field not used in this study were too fragmented to provide reliable measurements, due to predrilling fractures, drilling-induced fractures, and general degradation through time. Fracture density measurements are strongly dependent on the state of the core, and quantitative analysis was only performed on well-preserved core pieces exceeding 10 cm in length. Fractures induced by drilling and handling of the core were identified by their nonplanarity and lack of mineralization and are not included in the data set [*Kulander et al.*, 1990]. Each fracture is described by its location along the core, dimensions (height and length), orientation relative to the core axis, termination

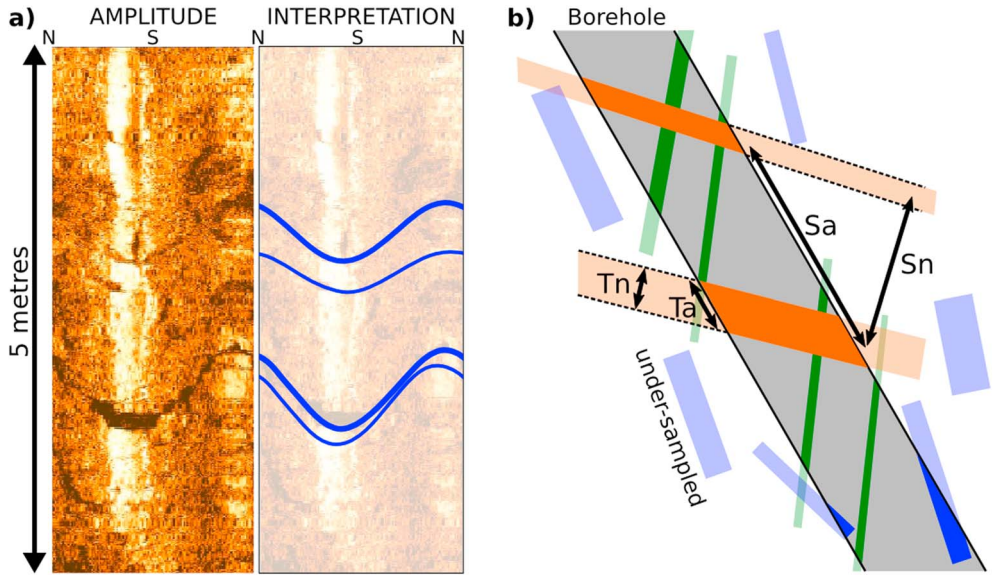

Figure 4. Example of a BHTV log and fracture measurements. (a) Unwrapped acoustic amplitude image oriented to north and interpretation of planar fractures appearing as sinusoids. (b) Schematic of an inclined borehole with three fracture sets (orange, green, and blue), showing measurements of apparent thickness (Ta) and spacing (Sa). Statistical analysis is performed on the fracture-normal thickness (Tn) and spacing (Sn). Fractures parallel to the borehole (blue set) are undersampled.

(intersection with other fractures or thinning), mineralization, thickness (between vein walls), and aperture (open space between fracture walls). Measurements were made on the outside of cylindrical cores, except in the case of RK27L2 where the core was slabbed. Most fractures observed on the slabbed core face were also seen on the outside of the core, and the resulting fracture density can be compared to non-slabbed cores. Fractures are partially to fully infilled with calcite, epidote, quartz, chlorite, other clays, Fe-oxide, and pyrite (Figure 3). Some fractures show slickenslides consistent with shear displacement. Further thin-section and crystallographic studies [e.g., *McNamara et al.*, 2016b] would be necessary to differentiate those fractures formed in opening and shearing mode.

3.2. BHTV Logs

The location, orientation, thickness, and acoustic amplitude is measured in BHTV logs for each fracture intersecting the borehole which has sufficient contrast with the background formation (Figure 4a) [*Massiot et al.*, 2015]. BHTV logs alone cannot differentiate between hydraulically conductive and non conductive fractures, so we use the term "thickness" instead of "aperture" to describe the distance between the two fracture walls. We use the term "fractures" to refer to discontinuities, including open fractures, faults with offsets, and veins, which the BHTV logs cannot discriminate.

At Rotokawa, three BHTV logs were acquired in boreholes RK18L2, RK30L1, and RK32 (Figure 2 and Table 1). *McNamara et al.* [2015] presented the structural and stress patterns in the Rotokawa Geothermal Field interpreted from these three BHTV logs. For the current study, we use the same data set with refined fracture thickness measurements.

The fracture analysis presented here focuses on intervals of andesite rocks (lavas and breccias), as defined from cuttings and inferred from the 3-D geological model of the Rotokawa Geothermal Field for intervals where drill cuttings were not recovered due to total drilling losses (Table 1) [*Wallis et al.*, 2013]. All planar features are considered as fractures. Andesite lavas may contain flow-banding, but these bands are thinner than the BHTV log resolution (~5 mm thick), and fractures can align with these flow-banding planes (Figure 3d). The planar feature orientations are also in agreement with them being fractures [*McNamara et al.*, 2015]. To limit the sampling effects caused by variable BHTV log quality, analysis is only conducted within zones of poor to good quality (i.e., where ≥25% of the circumference of the borehole was observed) [*Massiot et al.*, 2015]. Statistical analysis performed on zones of moderate to good quality (≥50% of the circumference of the borehole was observed) provided similar spacing and thickness distribution forms and parameters to those in zones of poor to good quality, albeit less well constrained due to reduced number of data points (see analysis

in the companion paper [*Massiot et al.*, 2017a], which uses the same data set). A total of 1133 fractures were sampled over a cumulative borehole interval of 2074 m (measured along the length of the deviated boreholes; Table 1 and Figure 2b).

In the absence of independent evidence allowing a stratigraphic refinement within andesitic sequence, analyses are made for each borehole and for a combined data set grouping all observations. The combined data set provides an average property, complementary to analyses made for each borehole, which can be used as a starting point for numerical heat and flow models typically having cells hundred meters wide. In addition, this combined data set has a better statistical significance than from individual boreholes, resulting from the higher number of input data.

4. Method

4.1. Fracture Processing

Relative to scientific drilling where continuous cores can be compared to image logs [e.g., *Genter et al.*, 1997], the data set available in the Rotokawa reservoir is typically sparse and required thorough statistical analysis to provide reliable interpretation.

Fracture sets of similar orientations are automatically delineated using K-means, fuzzy K-means, and agglomerative clusterings [*Hammah and Curran*, 1998; *James et al.*, 2013] and compared with fracture set delineation interpreted using Fisher density contours (see detailed analysis in *Massiot et al.* [2017a]). Here we briefly summarize the clustering techniques. The distance ("dissimilarity") measure used in the clustering algorithms is the acute angle between each pair of fractures. This dissimilarity measure is not affected by the 180° difference of dip direction for near-parallel subvertical fractures dipping in opposite directions. The best clustering configurations are based on a combination of a high silhouette width for the K-means clustering [*Reynolds et al.*, 2006], a high median membership level for the fuzzy K-means, and visual inspection of agglomerative clustering results [*Massiot et al.*, 2017a]. No fracture orientation analysis (absolute or relative) was possible in these non oriented cores, as core sections could only rarely be fitted together.

As is the case with one-dimensional scanline measurements made on outcrops, fractures subparallel to the borehole axes and cores are undersampled (Figure 4b). The orientation analysis of the BHTV data set is made after correction for this orientation bias [*Terzaghi*, 1965; *Massiot et al.*, 2015]. The fracture density of the BHTV and core data sets are reported for both the raw (uncorrected) data set, and after correction for the orientation bias (corrected data set). Analyses are made for the entire length of the borehole intersecting andesitic formations, similar to 1-D scanlines [e.g., *Gillespie et al.*, 1993]. Analysis of fracture distribution in the vicinity of faults such as presented by *Johri et al.* [2014] is not possible with the currently available data set. Indeed, there is only one documented intersection of a fault with a borehole where a BHTV log was acquired, but the precise fault location is uncertain [*Wallis et al.*, 2013; *McNamara et al.*, 2015]. On the contrary, localized variations of dip direction and S_{Hmax} rotations along the boreholes suggest that minor faults are present in the vicinity of the boreholes, in addition to the three large faults [*McNamara et al.*, 2015]. As independent data identifying such minor faults lack to date, the results presented in this work are representative of the rock mass as a whole.

The apparent fracture thickness measured at the borehole wall is converted to the true fracture thickness measured perpendicular to the fracture walls (Figure 4b) [*Barton and Zoback*, 1992; *Massiot et al.*, 2015]. Fracture spacing is measured for each fracture set between adjacent fractures along the borehole. This apparent fracture spacing is converted into the fracture-normal spacing, perpendicular to the mean orientation of the fracture set [*Priest*, 1993]. Fracture attributes are generally subject to sampling bias due to their size, with the undersampling of small values due to the resolution of the data set, and undersampling of large values due to their scarcity [*Pickering et al.*, 1995]. At Rotokawa, the fracture thickness population is considered to be fully sampled between 9 and 30 mm, and the fracture spacing between 0.03 and 30 m [*Massiot et al.*, 2017a]. Due to drilling wear of the borehole wall and scattering of the acoustic signal at the fracture edges, thickness values may be slightly overestimated.

4.2. Distribution Fitting

The probability distribution form and parameters of the fracture thickness and spacing are evaluated following methods described in *Massiot et al.* [2017a] and summarized briefly herein. Five probability distributions commonly found in geological systems, namely, negative exponential, lognormal, gamma, power law, and power exponential [*Bonnet et al.*, 2001], are fitted to the fracture thickness or spacing populations within

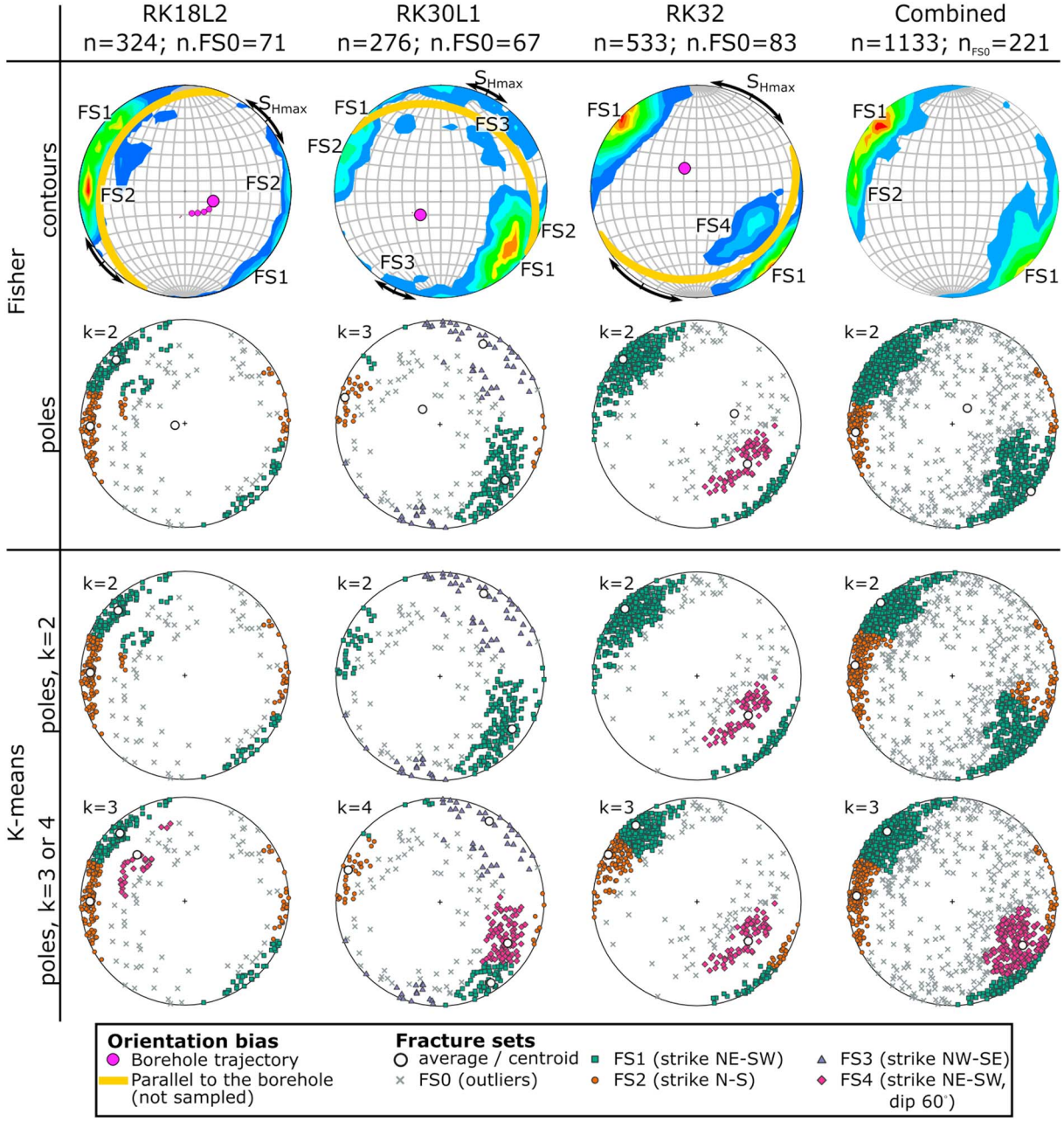

Figure 5. Fracture set orientations in the Rotokawa andesites for each of the three BHTV logs and for the combined boreholes. Distribution fitting of fracture thickness and spacing were tested on all configurations. (top) Fisher contouring (colors represent percentages), S_{Hmax} orientation (mean value and one standard deviation) [*McNamara et al.*, 2015], and great circle with the orientation of poles to planes of fractures not sampled because they are parallel to the borehole (the pole of this great circle is the borehole trajectory); pole to planes separated into fracture sets. (bottom) Pole to planes separated in fracture sets using clustering algorithms. *n*: total fracture number; *n.FS0*: number of outliers; *k*: number of sets. All stereonets displayed as lower hemisphere Schmidt projection.

truncation bounds, i.e., where the data are inferred to be fully sampled. The fitting is made with maximum likelihood estimations applied to truncated distributions [*Stasinopoulos and Rigby*, 2007]. The power law distribution is estimated with a pareto distribution. Tests with maximum likelihood estimates of the power law coefficient [*Clauset et al.*, 2009] provided similar coefficients to the ones derived from the pareto distribution for data sets where the pareto (and hence power law) distribution was a good fit.

Akaike Information Criterion (AIC) and Schwartz Bayesian Criterion (SBC) statistical information criteria rank distributions by how well they approximate the data amongst the five tested distribution [*Burnham and Anderson*, 2002]. The difference ($\Delta(AIC_k) = AIC_k - AIC_{min}$) between the lowest AIC (AIC_{min}) and the AIC_k values

of an alternative distribution k decreases as the goodness of fit of the distribution k increases. We considered that models with $\Delta(AIC_k) < 5$ (referred to as "the AIC condition") represent the data similarly well following *Burnham and Anderson* [2002], although these authors evaluated that a threshold at $\Delta(AIC_k) > 2$ or 3 can be sufficient to conclude that models do not represent the data as well as the model with the lowest AIC. The same conditions are applied to SBC. Visual inspection of q-q plots ensures that the distributions satisfying the AIC or SBC condition are a good fit to the data in an absolute as well as relative way (see supporting information). AIC and SBC penalize distributions with numerous parameters (such as the power exponential distribution with three parameters $\hat{\mu}$, $\hat{\sigma}$, and $\hat{v}$) compared to those with fewer parameters (gamma, lognormal, and pareto distributions have two parameters $\hat{\mu}$ and $\hat{\sigma}$, and the exponential distribution has only one parameter $\hat{\mu}$). The penalty term for added parameters is higher for SBC than AIC. We use the AIC for ranking fracture spacing distributions spanning three orders of magnitude, and SBC for fracture thickness distributions spanning only half an order of magnitude in order to limit overfitting.

Fracture spacing is determined for each fracture set, and for each orientation clustering configuration (i.e., Fisher density contours and two configurations selected using K-means and agglomerative clustering; Figure 5 and section 5.1). Using three reliable and slightly different clustering configurations allows to test for the reliability of distribution fitting results. The spacing analysis is strengthened in cases where slightly different fracture sets yield similar spacing distribution results. Fracture thickness analysis is conducted for each borehole separately and combined, and for each fracture set in the combined data set. For each case, the distributions satisfying the AIC (or SBC for thickness) condition are listed in Tables 2 and 3, by decreasing AIC (or SBC) rank. Tables 2 and 3 also report the parameters of the distribution with the highest AIC rank [*Stasinopoulos and Rigby*, 2007; *Massiot et al.*, 2017a], and the power law coefficient derived from the fitted pareto distribution.

The power exponential distribution rarely satisfies the AIC condition and commonly has large confidence intervals for the $\hat{\sigma}$ parameters (>100 and commonly >1000 units with estimated values <30). To limit the risk of overfitting data sets with this three-parameter distribution, the power exponential distribution fits are not reported in the rest of the paper.

4.3. Density Calculations in Cores and BHTV Logs

Fracture abundance is evaluated here in three ways, corresponding to different dimensionalities of fractures and rock mass [*Dershowitz et al.*, 1999]: (1) P_{10} is the "linear density," defined as the number of fractures n per length of core or BHTV log L; (2) P_{32} is the "areal intensity," the sum of fracture area per volume of rock; and (3) P_{33} is the "volumetric porosity," the sum of fracture volume per volume of rock. P_{33}, expressed as a percentage, would correspond to the fracture porosity if fractures were open. P_{32} and P_{33} are often derived from outcrop measurements of the P_{21} fracture intensity (sum of fracture length per outcrop area) and stereological calculations to extrapolate from 2-D measurements to 3-D parameter [*Wang*, 2005]. Instead, the P_{32} and P_{33} values calculated in this work incorporate the weighting coefficients of each fracture used to mitigate the orientation sampling bias. Thus, the reported P_{32} and P_{33} values corrected for orientation bias are close to being a 3-D parameter.

P_{32} and P_{33} parameters are calculated for both the core and BHTV data sets, providing two scales of observation. Fractures are assumed to be planar, and their intersection with the cylindrical cores and boreholes form ellipses. The boreholes were overall close to being in gauge, as measured from the BHTV log [*Massiot et al.*, 2015], although independent confirmation by mechanical caliper log is lacking. We calculate P_{32} and P_{33} as if fractures were confined to the borehole. The areal intensity P_{32} is expressed as follows:

$$P_{32} = \frac{\sum_{i=1}^{n} \pi \cdot r \cdot a_i}{\pi \cdot r^2 \cdot L} = \frac{\sum_{i=1}^{n} a_i}{r \cdot L} \tag{1}$$

where a_i is length of the semimajor axis of the fracture i and r the core or borehole radius, i.e., the length of the semiminor axis of the ellipse representing the fracture. For the cores, the length of the major axis is measured along the fracture. The BHTV analysis automatically provides the length of the major axis.

P_{33}, the volume of fracture per volume of rock is

$$P_{33} = \frac{\sum_{i=1}^{n} \pi \cdot r \cdot a_i \cdot t_i}{\pi \cdot r^2 \cdot L} = \frac{\sum_{i=1}^{n} a_i \cdot t_i}{r \cdot L} \tag{2}$$

Table 2. Results of Probability Distribution Analysis of Fracture Spacing[a]

						Spacing			
FS	Borehole	Cl.	n	P_{10} (m^{-1})	Orient.	n*	Distribution	Parameters	$\hat{\alpha}$
1	All	F	728	0.35	90/311	697	LN(0)	0 [−0.1;0.1]/1.4 [1.3;1.4]	2.6 [2.3;3.1]
1	All	k2	605	0.29	90/316	579	LN(0)	0.2 [0.1;0.3]/1.4 [1.3;1.5]	2.5 [2.1;3]
1	All	k3/4	461	0.22	82/138	437	LN(0)	0.4 [0.3;0.6]/1.4 [1.3;1.5]	2.3 [1.9;2.8]
1	RK18L2	F	154	0.18	80/133	144	LN(0), Pa(1.5)	0.8 [0.5;1.1]/1.6 [1.3;1.8]	2.0 [1.4;3.3]
1	RK18L2	k2	132	0.16	79/136	123	LN(0), Pa(1.7)	1 [0.7;1.4]/1.6 [1.3;1.9]	1.8 [1.3;3.3]
1	RK18L2	k3/4	117	0.14	82/136	107	LN(0), Pa(1.0)	1.2 [0.7;1.7]/1.7 [1.3;2.1]	1.6 [1.2;3.3]
1	RK30L1	F	134	0.44	70/309	124	LN(0), Pa(2.6), Ga(3.7)	−0.3 [-0.6;0]/1.4 [1.2;1.6]	2.6 [1.8;4]
1	RK30L1	k2	162	0.53	76/303	148	LN(0), Pa(1.2)	−0.5 [-0.7;-0.3]/1.4 [1.2;1.6]	2.7 [2;3.8]
1	RK30L1	k3/4	52	0.17	80/328	47	Ga (0), LN(1.6), Pa(2.8)	3.6 [2.3;5.8]/1.5 [1.1;2.1]	1.3 [1;5.9]
1	RK30L1	F, k2,	380	0.41	84/131	373	LN(0)	0.1 [−0.1;0.2]/1.3 [1.2;1.4]	3.2 [2.5;4.2]
1	RK30L1	k3/4	241	0.26	83/143	233	LN(0)	0.5 [0.3;0.6]/1.4 [1.2;1.5]	2.4 [1.9;3.3]
2	All	F	113	0.05	83/086	94	Pa(0), LN(2.4)	0.2 [1.7;9.7]/4.1 [1.6;10.8]	1.2 [1.1;1.6]
2	All	k2	236	0.11	86/096	213	Pa(0), LN(4.1)	0.2 [3.4;11.9]/6.3 [2.3;17.2]	1.2 [1.1;1.4]
2	All	k3/4	190	0.09	83/094	163	Pa(0), LN(3.7)	0.2 [2.2;8.1]/4.2 [2;9.1]	1.2 [1.1;1.5]
2	RK18L2	F	101	0.12	80/088	88	Pa(0), LN(3.1)	0.2 [1;4.9]/2.3 [1.2;4.3]	1.4 [1.2;1.8]
2	RK18L2	k2	123	0.15	81/091	108	Pa(0), LN(2.0)	0.3 [0.9;4]/1.9 [1.1;3.3]	1.5 [1.3;1.9]
2	RK18L2	k3/4	117	0.14	83/091	103	Pa(0), LN(1.5)	0.3 [0.8;3.4]/1.7 [1.0;2.8]	1.6 [1.4;2]
2	RK30L1	F	28	0.09	83/106	22	Pa(0), LN(0.1), Ga(0.7), Ex(3.9)	0.7 [0;∞]/7.5 [0;∞]	1.1 [1;∞]
2	RK30L1	k3/4	30	0.10	82/108	24	LN(0), Pa(0.1), Ga(0.4)	1.4 [−0.8;3.5]/2.4 [1;5.8]	1.1 [1;10^{42}]
2	RK32	k3/4	139	0.15	86/116	132	LN(0), Pa(3.5)	0.8 [0.4;1.1]/1.5 [1.3;1.8]	2 [1.3;3.6]
3	RK30L1	F	51	0.17	77/209	42	Ga(0), LN(0), Pa(0.7)	3.2 [1.9;5.3]/1.5 [1.1;2.1]	1.4 [1.1;2.8]
3	RK30L1	k2	51	0.17	77/209	42	LN(0), Ga(0), Pa(0.7)	0.4 [−0.3;1.1]/1.8 [1.3;2.5]	1.4 [1.1;2.8]
3	RK30L1	k3/4	48	0.16	76/212	39	Ga(0), LN(0.3), Pa(0.8)	3.6 [2;6.2]/1.6 [1.1;2.2]	1.3 [1;2.9]
4	All	k3/4	190	0.09	67/303	161	LN(0), Pa(0.6)	0.4 [0.1;0.8]/1.8 [1.5;2.1]	1.5 [1.3;1.9]
4	RK18L2	k3/4	21	0.02	50/133	11	LN(0), Pa(0.3), Ex(0.7), Ga(1.9)	1.9 [−0.3;4.1]/1.5 [0.7;3.2]	1.1 [1;2.10^{25}]
4	RK30L1	k3/4	83	0.27	64/297	75	Ga(0), LN(0.5), Pa(2.0)	2.4 [1.8;3.4]/1.4 [1.1;1.7]	2.0 [1.4;3.5]
4	RK32	F, k2, k3/4	70	0.08	52/308	60	Pa(0), LN(1.1), Ga(4.9)	0.3 [1.3;21.6]/5.3 [0.6;49.2]	1.2 [1;2.8]

[a]FS: fracture set number; Cl.: clustering configuration, either by Fisher contours (F) or with K-means (k2: 2 clusters; k3/4: 3 or 4 clusters; Figure 5); n: number of fractures per fracture set; P_{10}: linear density (not corrected for orientation sampling bias). Orient.: mean orientation (dip magnitude/dip direction); n*: number of fracture after truncations for sampling bias; $\hat{\alpha}$: power law coefficient derived from the pareto distribution. The listed distributions satisfy the AIC condition ($\Delta(AIC) < 5$) and are listed by decreasing goodness of fit, i.e., with increasing AIC score, the latter indicated in brackets. Ex: exponential; Ga: gamma; LN: lognormal; Pa: pareto. Listed distribution parameters and 95% confidence intervals are those of the highest AIC rank distribution, and displayed as $\hat{\mu}/\hat{\sigma}$ according to the number of parameters of each distributions (probability distribution formulas in *Stasinopoulos and Rigby* [2007] and *Massiot et al.* [2017a]).

Table 3. Results of Probability Distribution Analysis of Fracture Thickness[a]

					Thickness			
FS	Borehole	Cl.	n	Orient.	n*	Distribution	Parameters	$\hat{\alpha}$
All	All	F, k2, k3/4	1132	90/116	597	Ex(0)	6.1 [5.5;6.8]	2.6 [2.4;2.8]
All	RK18L2	F, k2, k3/4	324	78/110	104	Ex(0), LN(3.4), Ga(4.1)	3.2 [2.7;3.9]	4.3 [4.3;4.4]
All	RK30L1	F, k2, k3/4	275	74/285	124	Ex(0), Ga(4.8), LN(4.8)	3.8 [3.2;4.6]	3.8 [1.5;16.5]
All	RK32	F, k2, k3/4	533	88/306	369	LN(0), Ga(0.4), Ex(2.3)	2.6 [2.5;2.7]/0.4 [0.4;0.6]	1.9 [1.6;2.2]
1	All	k2	605	90/316	333	Ex(0), LN(4.5)	6.0 [5.3;6.9]	2.6 [2.3;2.9]
1	All	k3/4	461	82/138	256	Ex(0), LN(4.8)	6.1 [5.2;7.1]	2.6 [2;3.5]
2	All	k2	236	86/96	104	Ex(0), Pa(2.9), LN(3.2), Ga(4.0)	5.5 [4.2;7.1]	2.9 [2.4;3.7]
2	All	k3/4	190	83/94	74	Ex(0), Pa(3.0), LN(3.2), Ga(3.9)	5.0 [3.7;6.7]	3.1 [2.4;4.3]
4	All	k3/4	190	67/303	107	Ex(0), Ga(4.5), LN(4.6)	6.1 [4.8;7.8]	2.6 [2;3.4]

[a]Distribution ranking uses SBC. Same nomenclature as Table 2.

where t_i is the thickness of fracture i. In the following, we describe P_{10} and P_{33}; P_{32} values presented in Table 1 can be used for further fracture modeling.

Siratovich et al. [2014] measured P_{10} on thin sections by counting the number of cracks that intersected a grid array of parallel and perpendicular lines that were spaced at 0.1 mm. Then, they derived the P_{32} from the P_{10} measured in two orthogonal directions and stereological considerations. Finally, we derived P_{33} assuming a 5 μm mean fracture thickness (P. Siratovich, personal communication, 2016).

5. Results

5.1. Orientation

K-means clustering of fracture orientation identified in the BHTV logs, supported by fuzzy K-means and agglomerative clustering, yields four fracture sets (FS1 to FS4; see detailed analysis in *Massiot et al.* [2017a]). For each borehole and the combined data set, there are two best configurations: (1) with two fracture sets and (2) with either three or four fracture sets (Figure 5).

FS1, FS2, and FS3 are steeply dipping (mean dip magnitudes of 76–90°, 80–86°, and 77°, respectively), and strike NE-SW, N-S, and NW-SE, respectively (Tables 2 and 3). FS4 strikes NE-SW like FS1, but with a moderate dip (70° average). FS1 is the dominant orientation, with a strike parallel to the maximum horizontal stress direction (S_{Hmax}) [*Seebeck et al.*, 2014a; *McNamara et al.*, 2015] and is observed in all three boreholes. FS2 is most evident in borehole RK18L2, with slightly fewer fractures than in FS1 (Table 2). Fractures of FS2 orientation are sparsely observed in boreholes RK30L1 and only identified as a separate fracture set in borehole RK32 in the clustering configuration with three fracture sets. FS3 is observed only in borehole RK30L1. FS4 is considered to form a separate set from FS1 in borehole RK32 rather than stemming from an observation bias, because it contains a large number of fractures dipping ~60° (see Figure 5, where the loci of poles to fractures parallel to each borehole not sampled by the BHTV log are presented as great circles). FS4 is also separated from FS1 by clustering algorithms in boreholes RK18L2 and RK30L1. In the combined data set which includes the three boreholes, FS1 and FS2 are dominant; FS4 is distinct from FS1 in the configuration with three fracture sets.

Fractures of FS1 and FS3 orientations are observed along the entire length of the boreholes. In contrast, 66% of fractures of FS2 orientation in borehole RK18L2 are located within 2195–2254 m, representing only 6% of the studied depth interval. Fractures of FS4 orientation are also located in specific intervals in borehole RK32 (82% within 2060–2110 m and 2420–2635 m representing together 29% of the studied depth interval), but not in the two other boreholes. The specific location of fractures of FS2 and FS4 orientations in boreholes RK18L2 and RK32, respectively, reinforces the inference that these two fracture sets are separate from FS1.

Delineation of fracture sets using Fisher contours yields similar configurations to those from clustering analysis, although the limits between fracture sets can differ slightly (Figure 5). For example, in borehole RK18L2, fractures striking NNE-SSW (between 015°–195° and 035°–215°) have a low membership level to FS1 and FS2 (<90%) [*Massiot et al.*, 2017a] and can thus be associated with either fracture set. Similarly, the separation of FS2 from FS1 in borehole RK30L1 using Fisher contours is different from the one obtained by K-means clustering. In addition, such a configuration in borehole RK30L1 with three fracture sets made from Fisher contours is statistically less robust than with either two or four fracture sets (see discussion in *Massiot et al.* [2017a]).

Fracture sets are well clustered, with high (≥0.9) cluster intensity (measured by the resultant of the mean vector which varies from 0 for a non clustered set, to 1 for a single orientation). The only exceptions are for borehole RK30L1 where cluster intensity is 0.5 for FS1 in the configuration with two fracture sets, and 0.7 for FS3 delineated from Fisher contours. The spacing of outliers (<1% Fisher density, named *FS0* in Figure 5) is not analyzed as these fractures do not have a clear mean orientation (cluster intensities are <0.5).

Borehole RK18L2 has more fractures dipping toward the NW than the other two boreholes, and the dominant dip direction varies along the boreholes. However, the strike orientations of each fracture set are similar between boreholes, and average dip magnitudes of fracture sets FS1, FS2, and FS3 are commonly >80° (Table 2), which justifies studying the spacing for fracture sets comprising both dip directions. We refer the reader to *McNamara et al.* [2015] for a detailed discussion of the variations of dip direction and fracture densities in the three boreholes.

5.2. Spacing

Fracture spacing for individual fracture sets in BHTV logs varies between 0.01 and 165.03 m with an average of 3.4 m, standard deviation of 9.4 m, and a median of 1.1 m. The highest AIC ranking distribution for

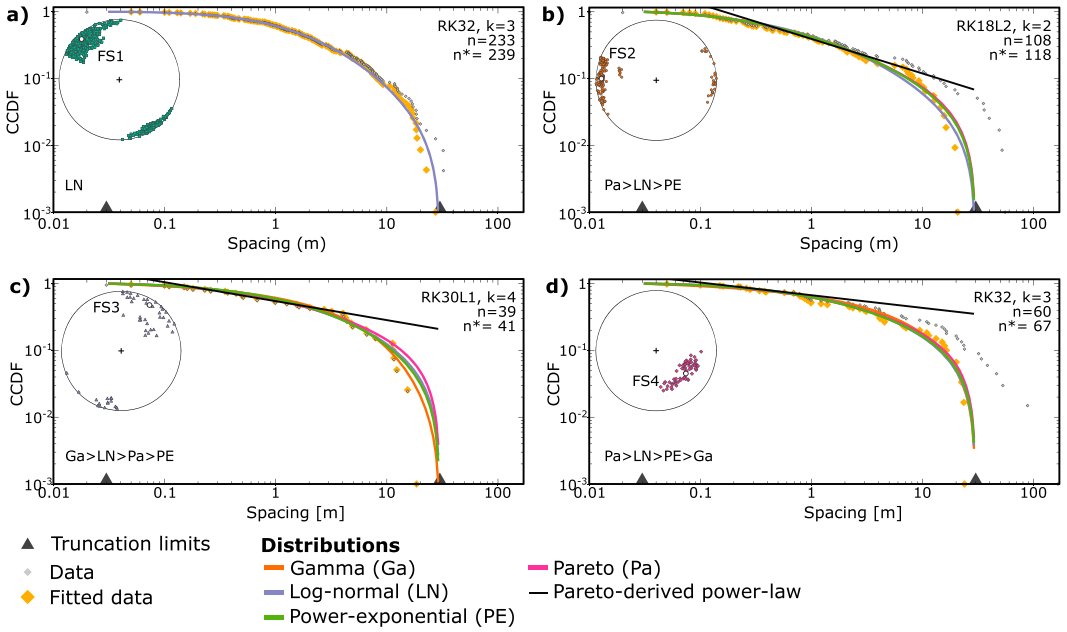

Figure 6. Examples of complementary cumulative density function (CCDF) and probability distributions satisfying the AIC condition for the spacing of each fracture set, listed by decreasing AIC rank. (a) FS1 in borehole RK32 with three clusters. (b) FS2 in borehole RK18L2 with two clusters. (c) FS3 in borehole RK30L1 with four clusters. (d) FS4 in borehole RK32 with three clusters. The exponential distribution never satisfies the AIC condition and is not displayed. All displayed fracture sets are delineated with K-means clustering. The parameter values of the highest ranking distribution are listed in Table 2. *k*: number of clusters; *n*: number of fracture within truncation bounds used for the fitting; *n**: total number of fractures (without truncation).

fracture spacing within truncation limits (0.03–30 m) is lognormal for FS1; pareto for FS2; gamma or lognormal for FS3; and pareto, gamma, or lognormal for FS4 in boreholes RK32, RK30L1, and the combined data set, respectively (Table 2). The shapes of the complementary cumulative density function (CCDF) of fracture spacing on log-log coordinates reflect the differences evaluated with the AIC: the CCDF of FS1 and FS3 are curved (Figures 6a and 6c), whereas the CCDF of FS2 and FS4 have straight portions characteristic of power law distributions (Figures 6b and 6d).

Data sets with ≤233 fractures have alternate distributions also satisfying the AIC condition (Table 2). Fracture sets with fewer than 50 data points have four or five distributions satisfying the AIC condition because data are underconstrained [*Massiot et al.*, 2017a] and are thus of low confidence. Alternate distribution forms for fracture sets with 50–233 fractures are consistent between clustering configuration of each boreholes, which confirms they are not strictly caused by an arbitrary choice of clustering configuration. For FS1, alternate configurations to the lognormal distribution include the scale-independent power law distribution with Δ(AIC) of 1.0–2.6 for boreholes RK18L2 and RK30L1. On the contrary for FS2, alternate configurations to the power law distribution include the scale-independent lognormal distribution with Δ(AIC) of 2.0–3.1 for borehole RK18L2. While these Δ(AIC) are at the limit of being considered to similarly fit the data [*Burnham and Anderson*, 2002], the switch between the two distribution forms best fitting the datasets (lognormal followed by power law for FS1, and power law followed by lognormal for FS2 in borehole RK18L2) is considered significant.

The parameters of the lognormal distribution fitting FS1, where it has the highest ranking, are very similar for each borehole and the combined data set, with small 95% confidence intervals (Table 2). The power law coefficient ($\hat{\alpha}$) of FS2 in boreholes RK18L2 and the combined data set, where these distributions have the highest ranking, varies between 1.2 [1.1–1.4] (most likely value and 95% confidence interval) for the combined data set and 1.6 [1.4–2.0] for RK18L2. The lack of small spacing for FS2 (<0.1 m) suggests a high minimum bound of the power law exponent (Figure 6b). The power law coefficient is not constrained for borehole RK30L1 (<25 data points). For FS4, the power law coefficients vary between 1.2 [1.0–2.8] in RK32 and 2.0 [1.4–3.5] for RK30L1 and is not constrained for RK18L2 which has only 11 points.

A common way of determining the clustering tendency of a data set is to use the coefficient of variation (Cv) for normal distributions, the ratio of the spacing standard deviation to the mean spacing. Cv > 1 indicates a

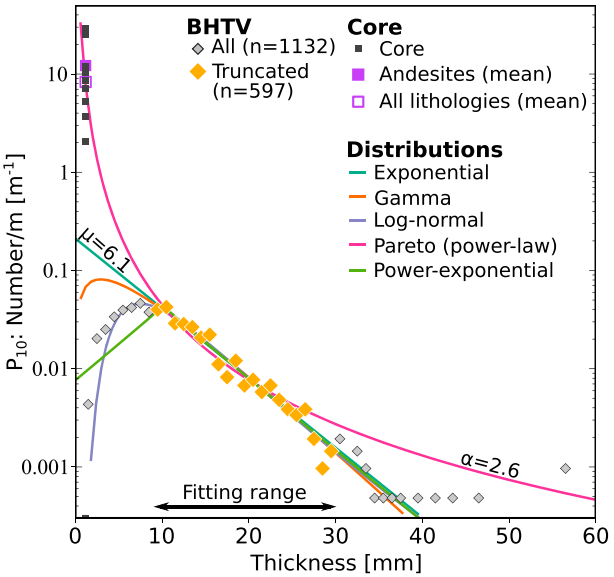

Figure 7. Histogram of the fracture thickness in BHTV logs and cores, normalized by the lengths of boreholes and cores, respectively, with probability distributions fitted to fracture thickness in BHTV logs between 9 and 30 mm. The exponential distribution appears as a straight line in this coordinate system.

clustered data set, while Cv = 1 indicates a randomly distributed data set and Cv < 1 an anticlustered data set [*Gillespie et al.*, 1999; *McCaffrey et al.*, 2003]. At Rotokawa, Cv of fracture spacings within truncation limits varies between 1.2 and 1.9, without clear correlation to specific fracture sets, which indicates that the fractures are slightly clustered. The Cv calculated for lognormal distributions [*Limpert et al.*, 2001] is ≥2 for all fracture sets, with a higher mean Cv for FS2 and FS4 (10 and 6.5, respectively) than for FS1 and FS3 (3 and 6, respectively). Although the precise Cv is dependent on the assumed underlying distribution (i.e., normal or lognormal), both sets of calculations suggest that fracture spacings are clustered.

5.3. Thickness

Fracture thicknesses in cores vary between 0.5 and 3 mm, with a mean of 1.2 ± 0.5 mm (one standard deviation). Overall, 70% of fractures in cores appear to be fully infilled, while the remaining 30% have openings of 0.2–2 mm, which usually varies along the fracture plane.

After correcting for the intersection angle between fractures and borehole, fracture thickness in the BHTV logs varies between 1 and 57 mm, with an average of 11 ± 7 mm. Within truncation limits (9–30 mm), exponential distributions have the highest SBC ranking for fracture thickness of the combined data set, each fracture set and each borehole, apart from borehole RK32 which is best approximated by a lognormal distribution (Table 3). The histogram of fracture thickness measured from BHTV logs appears as a straight line on a log-linear plot, in agreement with the highest SBC ranking of the exponential distribution (Figure 7) and shows the fitted distributions extended beyond the truncation limits [*Massiot et al.*, 2017a]. There are no other close contenders for the combined dataset containing 597 data points (Table 3). Other distributions satisfy the SBC condition for individual fracture sets: lognormal, and both lognormal and gamma distributions for FS1 and FS4, although with Δ(SBC) close to 5; and all distributions for fracture set FS2 which contains the smallest number of data points (<105) and are thus underconstrained [*Massiot et al.*, 2017a].

While the power law distributions estimated from BHTV data have poor SBC rankings compared to the other distribution forms, the power law distribution appears to fit the BHTV thickness data well between 9 and 27 mm and most importantly also fits the core data set (Figure 7). This histogram is normalized by the length of boreholes and cores, which allows comparison of the two data sets.

The exponential coefficient $\hat{\mu}$ fitted to the fracture thickness in BHTV logs varies between 3.2 [2.7–3.9] mm in borehole RK18L2 and 8.6 [7.4–10.0] mm in borehole RK32 (for which the exponential distribution is not the most likely), with a median of 6.1 mm (Table 1). The $\hat{\sigma}$ parameter of the gamma distributions is often close to 1 (between 0.5 and 1.5), which makes it similar to an exponential distribution. The power law coefficients $\hat{\alpha}$ vary between 1.9 [1.6–2.2] and 4.3 [4.3–4.4] with a median of 2.6.

5.4. Density

The linear fracture density P_{10} varies between cores (e.g., low in Figure 3a and high in Figure 3b and Table 1), and over short length scales on the same core (10–20 cm, Figure 3b). There is no correlation between fracture density and alteration intensity (Figure 8). Indeed, the highest and lowest P_{10} for andesite lava are both of moderate intensity, with two other cores of strong alteration intensity and two of weak alteration intensity having intermediate P_{10} values.

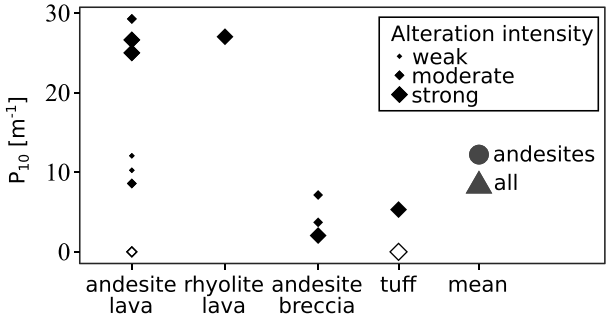

Figure 8. Linear fracture density (P_{10}) in cores as a function of the lithology and alteration intensity, for the data set not corrected for orientation bias ("raw" in Table 1). White symbols are for cores without any fractures. The mean densities are weighted by the length of each core for both the andesitic lithologies and all lithologies together, displayed as disk and triangle, respectively.

Amongst the few cores available, the P_{10} density in andesite breccias is lower (2 to 7.1 m^{-1}) than in the andesite lavas (8.6 to 29.3 m^{-1}), although a 0.7 m long core of andesite lava contains no discernible fractures. The core of rhyolite lava has a P_{10} density similar to those of andesite lavas. The two cores of tuff have low P_{10} of 5.3 m^{-1} in RK08, and no fractures in a 6.6 m long core in RK30L1. Fractures occupy 0–6.4% of the rock mass (P_{33} porosity uncorrected for orientation bias), although the upper bound of this range occurs over a short core (0.4 m long). The average uncorrected P_{33} in cores, weighted by the length of each core, is 0.9% for all lithologies, and 1.7% for just lavas and breccias. The 0.9–1.7 % P_{33} values for cores is a minimum, as results corrected for orientation sampling bias (see section 4.1) suggest that there are many more fractures in the rock mass than those observed (7% corrected P_{33} in lavas and breccias).

The mean P_{10} in BHTV logs is 0.5 m^{-1} and varies between 0.4 m^{-1} (for borehole RK18L2) and 0.9 m^{-1} (for borehole RK30L1; Table 1). The mean uncorrected P_{33} of 1.5 % for BHTV logs (weighted by the length of each borehole) is also larger when corrected for orientation bias (mean of 5.4%).

6. Discussion

6.1. Orientation and Spacing

As discussed by *McNamara et al.* [2015], BHTV-log scale fracture orientations at Rotokawa are controlled dominantly by quaternary tectonic stresses yielding dominant NE-SW striking normal faults, with possible influence of terrane sutures inferred in the Mesozoic greywacke basement (yielding possible N-S striking structures), fault linkage structures, accommodation zones between rift segments, and relays or bends in fault surfaces (yielding possible NW-SE striking structures). A similar dominant tectonic control on vein orientation is observed at Waihi, an andesite-hosted epithermal gold deposit located 140 km north of Rotokawa in the Coromandel peninsula (Figure 2a) [*Brathwaite et al.*, 2001; *Spörli and Cargill*, 2011]. Such epithermal deposits can be considered to some extent as fossil equivalents to active geothermal fields [*Rowland and Simmons*, 2012; *Simpson et al.*, 2015].

At Rotokawa, the spacings of fracture sets of different orientation are best approximated by different distribution forms. Although alternate distributions satisfy the AIC condition in cases, a change between the better fitting of scale-independent (power law) and scale-dependent (lognormal or gamma) distributions is observed, with sufficient AIC ranking differences [*Burnham and Anderson*, 2002]. Lognormal spacing of fracture set FS1 (NE-SW strike), with similar fitting parameters for the various clustering configurations (Table 2), and with no close contenders for borehole RK32, indicates a characteristic scale that may reflect the predominance of layering effects on fracture generation (Figure 1a) [*Gillespie et al.*, 1993; *Bonnet et al.*, 2001; *Schöpfer et al.*, 2011]. By contrast, the highest ranking distribution for spacings of sets FS2 (N-S strike) and FS4 in borehole RK32 (NE-SW strike, dipping ~60°) is power law and thus scale independent, with coefficients similar to those reported by *Gillespie et al.* [1993] for faults. Thus, spacing of these subordinate fracture set is likely controlled by rupture processes driven by anisotropic tectonic forces (Figure 1b) [*Bonnet et al.*, 2001; *McCaffrey et al.*, 2003]. While only three major subsurface faults have been identified with confidence at Rotokawa, the presence of other subsurface active faults has been inferred from localized S_{Hmax} direction rotations observed in BHTV logs [*McNamara et al.*, 2015] and may cause this power law spacing distribution locally. The limited number of FS3 fractures (NW-SE strike), observed only in RK30L1 borehole, precludes firm conclusions on its spacing (and location) controls.

The delineation of fracture sets at Rotokawa is complex because of the scatter of fracture orientation about mean orientations, as observable on Fisher density contours (Figure 5). Clustering orientation analysis provides strong support for the separation of FS2 from FS1 in borehole RK18L2, and FS4 from FS1 in

borehole RK32, and is confirmed by the different forms of the respective fracture spacing distributions. In addition, FS2 and FS4 orientations are compatible with the orientations expected for well-oriented faults given the regional tectonics. Finally, the preferential power law distribution for FS2 in borehole RK18L2 and FS4 in borehole RK32 is in agreement with the preferential depth at which these fractures occur in their respective boreholes (see section 5.1). On the contrary, spacing distribution of FS4 in boreholes RK18L2 and RK30L1 is dominantly lognormal, similar to FS1, which suggests that FS4 is a subset of FS1 in these two boreholes rather than a separate set controlled by different processes.

The scale dependence of fracture spacing of FS1, the dominant fracture set, is consistent with the nature of the reservoir host formation. Indeed, characteristic scales may result from stratification of the volcanic andesitic sequence, the finite dimensions (width, thickness, and length) of each lava flow, and the original jointing and flow-banding formed during cooling and emplacement of the lavas. In volcanic outcrops, autobreccias forming the external envelope of lava flows typically have high porosity and act as a mechanical interface, confining columnar joints within each lava flow [*DeGraff and Aydin*, 1987; *Hetényi et al.*, 2011; *Massiot et al.*, 2017b]. Together with hydrothermal breccias [*Rae*, 2007], lava flow margins may thus form mechanical interfaces within the Rotokawa reservoir. Although stratification of the Rotokawa andesites is not directly observed due to the lack of other characteristic borehole log and limited resolution of the cuttings, lognormal spacing distributions have also been found for veins in andesite-hosted epithermal gold deposits (at Waihi [*Brathwaite et al.*, 2001; *Spörli and Cargill*, 2011]; and Hishikari in Japan [*Sasaki*, 2006]). In the Waihi andesites, some veins tend to follow lava flow cooling joints, especially when the lavas are well jointed [*Brathwaite et al.*, 2001], similarly to thin dykes that partly follow cooling joints in lava flows [*Gudmundsson*, 2011].

In addition, flow-banding in Rotokawa andesites observed in places [*McNamara et al.*, 2016a, and references therein] may control fracture formation, such as in core RK04 where fractures are aligned with the vertical flow banding (Figure 3d; RK04 borehole is vertical). In New Zealand epithermal deposits, flow-banding influences the emplacement of hydrothermal breccias at Onemana [*Zuquim and Rowland*, 2013] but has only minor effects on vein emplacement at Waihi where strong silicification has homogenized the rock [*Brathwaite et al.*, 2001]. At Rotokawa, hydrothermal alteration may mechanically homogenize the volcanic sequence in places, but breccias and flow-banding may still produce mechanical interfaces which influence fracture propagation [*Misra et al.*, 2015]. The Rotokawa andesitic sequence as a whole may thus behave mechanically like sedimentary layered systems, in which non–power law joint spacing distributions are observed (Figure 1a) [*Ladeira and Price*, 1981; *Schöpfer et al.*, 2011].

In summary, fracture spacing results at Rotokawa suggest the superposition of (1) a pervasive network of fractures (FS1) whereby fracture location is influenced by the host rock stratification and (2) subordinate fracture sets (FS2 in borehole RK18L2, FS4 in borehole RK32) whereby fracture location is controlled by active faulting. A similar combination of exponential fracture spacing for host rock (with also has a characteristic scale) and power law spacing for fault rock has been documented in outcropping layered carbonates associated with normal and strike-slip faults [*Agosta et al.*, 2010]. The vein location distribution at Waihi is also inferred to have been controlled both by the initial jointing of the lava and by subsequent faulting events, especially close to faults where the lithological controls are overridden by tectonic controls [*Brathwaite et al.*, 2001; *Spörli and Cargill*, 2011]. Further, borehole (e.g., resistivity or microresistivity image logs [*Davatzes and Hickman*, 2010]) or near-borehole (e.g., vertical seismic profiling [*Place et al.*, 2011]) measurements would inform on the nature and thickness of these mechanical layers in the Rotokawa andesitic reservoir.

6.2. Thickness

Fracture thickness in BHTV logs is best approximated by an exponential distribution. The highest SBC rank of lognormal distribution in borehole RK32 is interpreted to reflect a sampling effect, with a possible higher left-truncation limit than in other boreholes. Conversely, the core data set, with fracture thicknesses one order of magnitude smaller than those observed from BHTV logs, matches the power law distribution obtained from the BHTV data (Figure 7). Three scaling relationships can explain these observations: either (1) the fractures at core (~1 mm-thick) and BHTV (~10 mm-thick) scales are related and follow the same power law distribution; or (2) the BHTV data set is approximated by an exponential distribution and is not related to the core data set; or (3) the thickness in BHTV log and cores follow the same exponential distribution, but the BHTV log detects only 2% of the 9–30 mm thick fractures intersecting the borehole.

Case 1 is the most likely, i.e., fracture thicknesses observed on cores and BHTV logs follow the same power law distribution. Distribution fitting of data sets spanning only half an order of magnitude is not well constrained

and explains why the SBC favors the distribution with only one parameter (exponential) rather than those with more parameters (including pareto). In addition, the power law distribution is the only one able to explain the occurrence (although rare) of fractures >40 mm-thick on the BHTV logs, above the truncation limit of the data. While some of these apparently thick fractures observed on BHTV logs may contain several thin fractures not resolved individually, >40 mm thick fractures have been observed in outcrop of epithermal deposits [*Brathwaite et al.*, 2001] and their presence within the Rotokawa andesites cannot be ruled out.

Case 2 is not supported by outcrop observations at Waihi, where vein thickness correlates positively with proximity to the main fluid source [*Brathwaite et al.*, 2001], rather than to a change of thickening processes between different scales. Similarly, measurements of fracture apertures at different and overlapping scales in mudstones and dolomites in the Sorrento Peninsula (Italy) are best modeled by a single power law distribution [*Guerriero et al.*, 2011]. Case 3 is also unlikely. Comparison of cores and BHTV logs in the Soultz geothermal field showed that 1 mm thick sealed fractures abundant in cores were beyond resolution of the BHTV logs, and this detection issue can mostly explain the difference of fracture density between the two data sets [*Genter et al.*, 1997]. Similar resolution limits of fracture thickness in BHTV logs have been inferred by *Barton and Zoback* [1992] at Cajon Pass (USA). These observations do not suggest significant undersampling of 9–30 mm thick fractures in BHTV logs, although direct comparison of core and BHTV logs over the same intervals, not available at Rotokawa, would be needed to test this assumption.

Power law coefficients of fracture thickness in BHTV logs at Rotokawa (2.6–3.1) are similar to the coefficients derived from BHTV log data for geothermal fields hosted in faulted crystalline formations [*Barton and Zoback*, 1992; *Radilla et al.*, 2012], and in andesites based on outcrop scanline measurements [*McCaffrey et al.*, 2003]. Fault zone thicknesses (0.01 – ~110 m thick) measured in tunnels in the south of the TVZ are also approximated by a power law distribution, with a coefficient of 1.5 and 1.8 in Miocene sandstone and mudstone, respectively [*Seebeck et al.*, 2014b]. While these latter coefficients are lower than those found at Rotokawa, they support the interpretation that fracture thickness measurements from core and BHTV logs at Rotokawa follow a single power law distribution at the measured scales and may extend to larger fracture sizes.

6.3. The 1-D and 3-D Fracture Abundances

The core and BHTV log data sample fracture thicknesses at two orders of magnitude: 1–3 mm in cores, and 1–57 mm in BHTV logs, although fractures <9 mm thick on BHTV logs are undersampled. Thin-section analysis by *Siratovich et al.* [2014] provides P_{10} and P_{32} measurements of ~5 μm thick fractures, and we derived P_{33} assuming a ~5μm mean fracture thickness (Figure 9b). The power law distribution approximating both core and BHTV log fracture thicknesses largely overestimates the linear density (P_{10}) observed for thin sections (Figure 9a; additional tests with P_{10} values not corrected for orientation bias also yield an overestimation of thin-section data). Fractures at thin-section, core, and BHTV log scales occupy a similar percentage of rock volume (P_{33}), with an average of 4.1%, 7%, and 5%, respectively (Table 1 and Figure 9b). As defined earlier, these volumes include veins, partially open fractures and open fractures.

The P_{10} measurements imply that fracture generation processes differ between the thin-section (10^{-6} m thick) and core (10^{-3} m thick) scales. A number of core and BHTV log intervals do not display any fractures, in contrast to the pervasive presence of fractures in available thin sections (most of the studied samples in *Siratovich et al.* [2014] did not have distinct macrofractures and include samples from core RK27L2#1 which has a low P_{10} at core scale). Most importantly, fractures observed in thin sections have an isotropic orientation and have been interpreted as being controlled by a uniform thermal stress experienced during the initial lava formation, burial, hydrothermal alteration, or drilling [*Siratovich et al.*, 2014]. While shear displacement of crystals within the lavas has been observed at thin-section scale [e.g., *Ramirez and Rae*, 2009], it is rare. The isotropic orientations of fractures at thin-section scales contrast with the dominant anisotropic orientation of fractures in BHTV logs and reservoir-scale faults which are strongly controlled by tectonic stresses. Although it is not clear whether fractures in cores have preferential orientations, due to the short length of available core fragments, the presence of slickenslides on some fracture faces suggests that these fractures are, at least in part, operating in shearing mode and controlled by tectonic stresses. Thus, the change between predominantly uniform (thermal) and anisotropic (tectonic) controls on fracture orientation and density, potentially associated with fracture coalescence and interactions, occurs at thickness scales intermediate between 10^{-6} and 10^{-3} m. However, the similar P_{33} at all three scales of observation suggests a self-similar fracture proportion of rock volume in 3-D. Further multiscale mechanical numerical modeling [*Schöpfer et al.*, 2011] combined with flow simulations at reservoir conditions [*Kissling et al.*, 2015] based on these measured

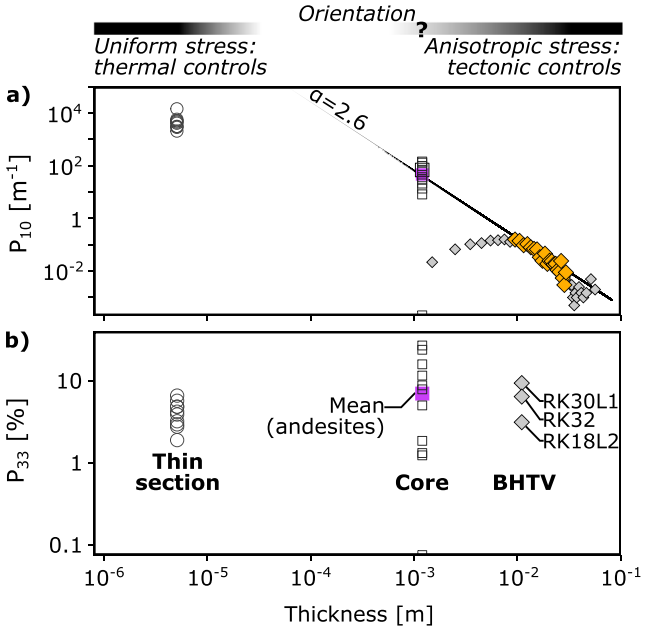

Figure 9. Fracture abundance for fractures in thin sections [*Siratovich et al.*, 2014], cores, and BHTV logs (Terzaghi-corrected data sets). (a) Linear density P_{10}. (b) Percentage of fracture volume within the rock mass (P_{33}). The thin-section values are plotted assuming a fracture thickness of ~5μm, also assumed to calculate P_{33} values. The symbology for core and BHTV log data are the same as in Figure 7.

densities may resolve the relative effects of the thermal, lithological, and tectonic controls on fracture geometries.

6.4. Effect of Lithology and Alteration on Fluid Pathways

The apparent lack of correlation between fracture density and alteration intensity observed in the limited cores available is consistent with results from microstructural measurements and laboratory experiments on samples of Rotokawa andesites [*Siratovich et al.*, 2014]. Indeed, the P_{32} values for fractures in thin sections appears to be independent of the alteration and mineralogy of the studied specimens. In addition, although the strength of the andesites decreases as the intensity of the alteration increases, brittle behavior still occurs in altered rocks under the pressure and temperature conditions representative of the Rotokawa reservoir [*Davidson et al.*, 2012; *Siratovich et al.*, 2014, 2016].

Some rhyolite breccias are (or are inferred to be) permeable in TVZ geothermal fields (e.g., Ohaaki [*Mroczek et al.*, 2016] and Wairakei [*Milloy and Lim*, 2012]). At Rotokawa, fracture density in cores is higher in lavas than in breccias. In breccias, the numerous veins observed surrounding clasts suggest that fluids can preferentially flow through open spaces along clast boundaries rather than through newly generated fractures in these high-strength rocks (60 to 211 MPa unconfined compressive strength) [*Siratovich et al.*, 2014; *Wyering et al.*, 2014]. Therefore, permeability in breccias relies on the interconnections of void space between clasts, and between clasts and rare fractures. The resulting fluid flow paths along clasts are more tortuous than those along subplanar fractures, and breccias with plugged pores potentially have lower permeability than fractured lavas as a result. It is unclear, however, how quickly the porosity between clasts becomes plugged by mineral precipitation, which impacts how much, and for how long, breccias can host permeability.

While tuff lithologies are not part of the main reservoir at Rotokawa, they affect shallow fluid circulations (>400 m below sea level) and connections between surface and reservoir [*Rae*, 2007]. The two cores of tuff studied here have low fracture density, including the RK30L1 core in which no fracturing was observed. This 6.6 m long core is strongly altered and has a porosity of 25–35% [*Rae et al.*, 2010], which is significantly higher than the typical porosity of <10% reported for andesites [*Siratovich et al.*, 2014]. In partially welded and strongly altered tuff lithologies, fluid flow is thus likely controlled primarily by matrix porosity rather than by fractures, even when strongly altered, as inferred at the Mokai and Ohaaki Geothermal Fields, TVZ [*Bignall et al.*, 2010; *Mroczek et al.*, 2016].

6.5. Potential Controls on Structural Permeability

Identifying which fracture characteristics control permeability is not straightforward in lava-hosted reservoirs where the fracture system geometry results from a combination of lithological, thermal, and past and present-day tectonic processes. For example, at the Karaha-Telaga Bodas Geothermal Field, Indonesia, permeable fractures are not the widest and are not necessarily located within high fracture density zones but are roughly perpendicular to σ_3 (minimum principal stress) and prone to slip under the modern stress regime [*Nemčok et al.*, 2004]. Similarly, as demonstrated by *McNamara et al.* [2015], permeable zones at Rotokawa contain fractures from each fracture set, some of the thickest fractures, some high-density fracture clusters, and some local in situ S_{Hmax} rotations inferred to be associated with slip on NE-SW and E-W striking active faults, but no one-to-one correlation between permeability and fracture attribute has been observed.

Critically stressed faults of high (>0.6) shear/normal stress ratio are generally considered to be dilatant and hydraulically conductive [*Barton et al.*, 1995; *Townend and Zoback*, 2000; *Barton et al.*, 2013]. Preliminary work on the Rotokawa stress field suggests that fractures of FS1 and FS4 orientations, and of FS2 orientation in specific stress ratio configurations, have high shear/normal stress ratio [*Davidson et al.*, 2012]. Further work is needed to explore this correlation, or lack thereof, between high shear/normal stress ratio and permeability.

Fracture connectivity, controlled by fracture density, length [*Bour and Davy*, 1998; *Bonnet et al.*, 2001], and orientation [*Kissling et al.*, 2015], can cause large variations in reservoir permeability at short scales (smaller than fracture length). In layered carbonate outcrops, *Agosta et al.* [2010] established a correlation between hydrocarbon flow and fracture connectivity, rather than density. At Rotokawa, intersections between the pervasive network of fractures of FS1 orientation, with fault-controlled fractures of FS2 and FS4 orientations in parts of the reservoir, may thus concentrate fluid flow.

In combination with a power law distribution for fault thickness, *Seebeck et al.* [2014b] documented in tunnels a power law relationship of fluid flow rates, where few "golden" thick, connected faults conduct the bulk of the fluids. Such a configuration at Rotokawa can also explain the observed compartmentalization, with closely located boreholes of high and low fluid productivity [*Hernandez et al.*, 2015] which would intersect, or not, one of these highly conductive faults. Flow models based on geometric fracture models at reservoir scale would help constrain the respective roles of fracture system geometry, stress, and water/rock interactions in controlling permeability. While only a small portion of the fractures described in this paper are permeable [*McNamara et al.*, 2015], a fracture and flow model of the Rotokawa reservoir would have to accommodate the fracture geometries described in thin-section, cores, and BHTV logs.

6.6. Modeling Rotokawa Fracture Systems at Reservoir Scale

Fracture orientation, spacing, thickness, and abundance reported in this paper can constrain geometrical fracture models of the Rotokawa reservoir and also in other andesite-hosted geothermal reservoirs (e.g., in Indonesia [*Nemčok et al.*, 2004]), especially those in exploration where borehole data is rare [*Pérez-Flores et al.*, 2017]. Geometrical models in andesite-hosted geothermal reservoirs can then support flow model development in reservoirs [*Berkowitz*, 2002]. Findings from the Rotokawa reservoir also inform on fracture systems in andesitic volcanoes [*Lachassagne et al.*, 2014; *Conway et al.*, 2015] or epithermal deposits [*Brathwaite et al.*, 2001] which form two possible end-members of the evolution of andesitic formations.

The power law thickness distribution evaluated at core and BHTV log scales may be extrapolated to predict the potential number of thicker fractures (>40 mm) and faults not resolved by the available reservoir data. The number of faults recognized in a reservoir typically increases as new wells are drilled in different parts (or depth) of the reservoir [*Massiot et al.*, 2011], so additional faults likely exist between current boreholes at Rotokawa. Extrapolating from borehole- to field-scale must, however, be done with caution. Power law distributions of fault sizes tend to have lower exponents when determined at seismic scale compared to outcrop scale, possibly due to a deviation from a power law relationship, or to different fault growth processes at different scales [*Nicol et al.*, 1996]. For example, large faults may be controlled by the average mechanical properties of the sequence in which they develop rather than by smaller-scale variations.

Fracture length cannot be measured on cores nor on the available BHTV logs. Probabilistic methods based on the proportion of fractures partially and fully intersecting the borehole [*Özkaya*, 2003] require full azimuthal coverage of the borehole on the BHTV log, which is rarely the case for the available logs acquired at Rotokawa. Evolving fracture models [*Davy et al.*, 2013] may constrain the fracture length distributions, although lithological controls on fracture growth would need to be included in the modeling. Outcrop-based analysis of fracture length in volcanic sequences [e.g., *Gudmundsson*, 2000] and near faults [e.g., *Vermilye and Scholz*, 1995; *Johnston and McCaffrey*, 1996] may be used to model fracture sets FS1 and FS2/FS4, respectively.

The choice of fracture aperture distribution and associated transmissivity is crucial for fluid flow and thermal modeling in geothermal systems. For example, numerical experiments demonstrate that a lognormal fracture aperture distribution channelizes heat depletion and hastens thermal breakthrough, while a constant aperture distribution uniformly extracts heat from the system [*Doe et al.*, 2014]. At Rotokawa, only 30% of fractures in cores have an opening discernible with the naked eye, and in most cases this opening is not constant along the fracture plane, so the results presented here for fracture thickness cannot be directly related to fracture aperture. In addition, fracture aperture is sensitive to fracture roughness [*Ishibashi et al.*, 2014], confining pressure [*Chen et al.*, 2000; *Barton et al.*, 2013] and pore pressure [*Hickman et al.*, 1995, and references therein].

Given the uncertainty of fracture length and hydraulic aperture, and the possibility that several distribution forms can be fitted to the spacing and thickness data presented here, future fracture and flow models should reflect these uncertainties.

7. Conclusion

Statistical analysis of fracture attributes at several scales of observations constrains the geometry of the Rotokawa fracture system, which is a necessary input into geologically informed reservoir models and improved understanding of fluid pathways in such andesite-hosted geothermal systems. Fracture orientation, spacing and density suggest a combination of tectonic, lithological, and thermal controls on the geometry of the fracture system. At the BHTV log scale, the dominant fracture population has a scale-dependent lognormal fracture spacing, interpreted to be related to stratification within the lava sequence, individual lava flow size, or inherited jointing. In contrast, scale-independent power law spacing of subordinate fracture populations are interpreted to be controlled by tectonic stresses and associated faults. Fracture thickness is approximated by a power law distribution spanning 1.5 orders of magnitude (1–40 mm thick), which may extend to larger fault sizes (100 m thick). However, this power law does not continue to thin-section scale (~5 μm thick) fractures, reinforcing previous interpretation that these pervasive fractures with isotropic orientations are likely dominantly controlled by thermal stresses, rather than anisotropic tectonic stresses as observed at BHTV log and reservoir scales. Fracture volumes, including closed veins, of ~5% of the rock mass are similar at thin-section, core, and BHTV log scales, suggesting a self-similar behavior in 3-D. The potential effects of hydrothermal alteration, host lithology (lava or breccia), and fracture transmissivity in the current stress field on reservoir-scale flow pathways have been evaluated qualitatively as a base for further quantitative analysis.

Acknowledgments

We thank N. Davatzes, J. Rowland, and M. Savage for their constructive advice, and the Rotokawa Joint Venture (Mercury New Zealand and Tauhara North No.2 Trust) for allowing publication of this work. This project forms part of the first author's PhD thesis funded by the Sarah Beanland Memorial Scholarship awarded by GNS Science. Additional support was provided by the GNS Science's "Geothermal Resources of New Zealand" research program. We thank Judith Sausse and an anonymous reviewer for their helpful reviews of this work. Data used in this paper and in the companion manuscript [*Massiot et al.*, 2017a] are provided in the supporting information.

References

Ackermann, R. V., R. W. Schlische, and M. O. Withjack (2001), The geometric and statistical evolution of normal fault systems: An experimental study of the effects of mechanical layer thickness on scaling laws, *J. Struct. Geol.*, *23*(11), 1803–1819, doi:10.1016/s0191-8141(01)00028-1.

Agosta, F., M. Alessandroni, M. Antonellini, E. Tondi, and M. Giorgioni (2010), From fractures to flow: A field-based quantitative analysis of an outcropping carbonate reservoir, *Tectonophysics*, *490*(3–4), 197–213, doi:10.1016/j.tecto.2010.05.005.

Alemdag, S. (2015), Assessment of bearing capacity and permeability of foundation rocks at the Gumustas Waste Dam Site (NE Turkey) using empirical and numerical analysis, *Arabian J. Geosci.*, *8*(2), 1099–1110, doi:10.1007/s12517-013-1236-3.

André-Mayer, A.-S., and J. Sausse (2007), Thickness and spatial distribution of veins in a porphyry copper deposit, Rosia Poieni, Romania, *J. Struct. Geol.*, *29*(10), 1695–1708, doi:10.1016/j.jsg.2007.06.010.

Aprilina, N. V., D. Y. Satya, S. Rejeki, G. Golla, and M. Waite (2015), Geologic modeling workflow for volcanic hosted geothermal reservoirs: Case Study from Salak geothermal field, paper presented at the World Geothermal Congress, Melbourne, Australia, 19-25 April.

Arnórsson, S. (1995), Geothermal systems in Iceland: Structure and conceptual models—I. High-temperature areas, *Geothermics*, *24*(5–6), 561–602, doi:10.1016/0375-6505(95)00025-9.

Barton, C. A., and M. D. Zoback (1992), Self-similar distribution and properties of macroscopic fractures at depth in crystalline rock in the Cajon Pass Scientific Drill Hole, *J. Geophys. Res.*, *97*(B4), 5181–5200, doi:10.1029/91JB01674.

Barton, C. A., M. D. Zoback, and D. Moos (1995), Fluid flow along potentially active faults in crystalline rock, *Geology*, *23*(8), 683–686, doi:10.1130/0091-7613(1995)023<0683:FFAPAF>2.3.CO;2.

Barton, C. A., D. Moos, L. Hartley, S. Baxter, L. Foulquier, H. Holl, and R. Hogarth (2013), Geomechanically coupled simulation of flow in fractured reservoirs, paper presented at the 38th Workshop on Geothermal Engineering, Stanford Univ., Calif., 11–13 Feb.

Begg, J. G., and V. Mouslopoulou (2010), Analysis of late Holocene faulting within an active rift using lidar, Taupo Rift, New Zealand, *J. Volcanol. Geotherm. Res.*, *190*(1–2), 152–167, doi:10.1016/j.jvolgeores.2009.06.001.

Berkowitz, B. (2002), Characterizing flow and transport in fractured geological media: A review, *Adv. Water Resour.*, *25*(8–12), 861–884, doi:10.1016/s0309-1708(02)00042-8.

Bignall, G., A. J. Rae, and M. Rosenberg (2010), Rationale for targeting fault versus formation-hosted permeability in high-temperature geothermal systems of the Taupo Volcanic Zone, New Zealand, paper presented at the World Geothermal Congress, World Geothermal Congress, 25-29 April.

Bonnet, E., O. Bour, N. E. Odling, P. Davy, I. Main, P. Cowie, and B. Berkowitz (2001), Scaling of fracture systems in geological media, *Rev. Geophys.*, *39*(3), 347–383, doi:10.1029/1999RG000074.

Bour, O., and P. Davy (1998), On the connectivity of three-dimensional fault networks, *Water Resour. Res.*, *34*(10), 2611–2622, doi:10.1029/98WR01861.

Brathwaite, R. L., H. J. Cargill, A. B. Christie, and A. Swain (2001), Lithological and spatial controls on the distribution of quartz veins in andesite- and rhyolite-hosted epithermal Au-Ag deposits of the Hauraki Goldfield, New Zealand, *Mineral. Deposit.*, *36*(1), 1–12, doi:10.1007/s001260050282.

Browne, P., I. Graham, R. Parker, and C. Wood (1992), Subsurface andesite lavas and plutonic rocks in the Rotokawa and Ngatamariki geothermal systems, Taupo Volcanic Zone, New Zealand, *J. Volcanol. Geotherm. Res.*, *51*(3), 199–215, doi:10.1016/0377-0273(92)90123-u.

Burnham, K. P., and D. R. Anderson (2002), *Model Selection and Multimodel Inference: A Practical Information-Theoretic Approach*, 2nd ed., Springer, New York.

Chambefort, I., B. Lewis, C. Wilson, A. Rae, C. Coutts, G. Bignall, and T. Ireland (2014), Stratigraphy and structure of the Ngatamariki geothermal system from new zircon U-Pb geochronology: Implications for Taupo Volcanic Zone evolution, *J. Volcanol. Geotherm. Res.*, *274*, 51–70, doi:10.1016/j.jvolgeores.2014.01.015.

Chen, R.-H., C.-H. Lee, and C.-S. Chen (2001), Evaluation of transport of radioactive contaminant in fractured rock, *Environ. Geol.*, *41*(3–4), 440–450, doi:10.1007/s002540100410.
Chen, Z., S. Narayan, Z. Yang, and S. Rahman (2000), An experimental investigation of hydraulic behaviour of fractures and joints in granitic rock, *Int. J. Rock Mech. Mining Sci.*, *37*(7), 1061–1071, doi:10.1016/s1365-1609(00)00039-3.
Chilès, J. P. (2005), Stochastic modeling of natural fractured media: A review, in *Geostatistics Banff 2004*, pp. 285–294, Springer, Dordrecht, Netherlands.
Clauset, A., C. R. Shalizi, and M. E. J. Newman (2009), Power-law distributions in empirical data, *Soc. Indust. Appl. Math. Rev.*, *51*(4), 661–703, doi:10.1137/070710111.
Conway, C. E., D. B. Townsend, G. S. Leonard, C. J. N. Wilson, A. T. Calvert, and J. A. Gamble (2015), Lava-ice interaction on a large composite volcano: A case study from Ruapehu, New Zealand, *Bull. Volcanol.*, *77*(3), 21, doi:10.1007/s00445-015-0906-2.
Davatzes, N. C., and S. H. Hickman (2010), Stress, fracture, and fluid flow analysis using acoustic and electrical image logs in hot fractured granites of the Coso Geothermal Field, California, U.S.A., in *Dipmeter and Borehole Image Log Technology: AAPG Memoir 92*, edited by M. Poppelreiter, C. Garcia-Carballido, and M. Kraaijveld, pp. 259–293, AAPG Spec. Volumes, doi:10.1306/13181288M923134.
Davidson, J., P. A. Siratovich, I. C. Wallis, D. M. Gravley, and D. D. McNamara (2012), Quantifying the stress distribution at the Rotokawa Geothermal Field, New Zealand, paper presented at the 34th New Zealand Geothermal Workshop, Auckland, New Zealand, 19-21 Nov.
Davy, P., R. L. Goc, and C. Darcel (2013), A model of fracture nucleation, growth and arrest, and consequences for fracture density and scaling, *J. Geophys. Res. Solid Earth*, *118*, 1393–1407, doi:10.1002/jgrb.50120.
DeGraff, J. M., and A. Aydin (1987), Surface morphology of columnar joints and its significance to mechanics and direction of joint growth, *Geol. Soc. Am. Bull.*, *99*(5), 605–617, doi:10.1130/0016-7606(1987)99<605:SMOCJA>2.0.CO;2.
Dershowitz, B., T. Eiben, S. Follin, and J. Andersson, (1999), SR 97-Alternative models project. Discrete fracture network modelling for performance assessment of Aberg, *Tech. Rep.*, Swedish Nuclear Fuel and Waste Management Co., Stockholm.
Doe, T., R. Mclaren, and W. S. Dershowitz (2014), Discrete fracture network simulations of enhanced geothermal systems, paper presented at the Thirty-Ninth Workshop on Geothermal Reservoir Engineering, Stanford Univ., Stanford, Calif., 24-26 Feb.
Feng, Z.-Q. (2008), Volcanic rocks as prolific gas reservoir: A case study from the Qingshen gas field in the Songliao Basin, NE China, *Mar. Pet. Geol.*, *25*(4–5), 416–432, doi:10.1016/j.marpetgeo.2008.01.008.
Genter, A., C. Castaing, C. Dezayes, H. Tenzer, H. Traineau, and T. Villemin (1997), Comparative analysis of direct (core) and indirect (borehole imaging tools) collection of fracture data in the Hot Dry Rock Soultz reservoir (France), *J. Geophys. Res.*, *102*(B7), 15,419–15,431, doi:10.1029/97JB00626.
Gillespie, P., C. Howard, J. Walsh, and J. Watterson (1993), Measurement and characterisation of spatial distributions of fractures, *Tectonophysics*, *226*(1–4), 113–141, doi:10.1016/0040-1951(93)90114-y.
Gillespie, P. A., J. D. Johnston, M. A. Loriga, K. J. W. McCaffrey, J. J. Walsh, and J. Watterson (1999), Influence of layering on vein systematics in line samples, *Geol. Soc. London Spec. Publ.*, *155*(1), 35–56, doi:10.1144/gsl.sp.1999.155.01.05.
Gudmundsson, A. (2000), Fracture dimensions, displacements and fluid transport, *J. Struct. Geol.*, *22*(9), 1221–1231, doi:10.1016/S0191-8141(00)00052-3.
Gudmundsson, A. (2011), Deflection of dykes into sills at discontinuities and magma-chamber formation, *Tectonophysics*, *500*(1–4), 50–64, doi:10.1016/j.tecto.2009.10.015.
Gudmundsson, A., I. Fjeldskaar, and S. L. Brenner (2002), Propagation pathways and fluid transport of hydrofractures in jointed and layered rocks in geothermal fields, *J. Volcanol. Geotherm. Res.*, *116*(3–4), 257–278, doi:10.1016/S0377-0273(02)00225-1.
Guerriero, V., S. Vitale, S. Ciarcia, and S. Mazzoli (2011), Improved statistical multi-scale analysis of fractured reservoir analogues, *Tectonophysics*, *504*(1–4), 14–24, doi:10.1016/j.tecto.2011.01.003.
Hammah, R., and J. Curran (1998), Fuzzy cluster algorithm for the automatic identification of joint sets, *Int. J. Rock Mech. Min. Sci.*, *35*(7), 889–905, doi:10.1016/s0148-9062(98)00011-4.
Hansen, B., and J. Buczak (2010), Making interpretable images from image logs, in *Dipmeter and Borehole Image Log Technology: AAPG Memoir 92*, edited by M. Poppelreiter, C. Garcia-Carballido, and M. A. Kraaijveld, pp. 51–66, AAPG, doi:10.1306/13181277M923405.
Hernandez, D., J. Clearwater, J. Burnell, P. Franz, L. Azwar, and A. Marsh (2015), Update on the modeling of the Rotokawa geothermal system: 2010–2014, in *Proceedings of the World Geothermal Congress*, Melbourne, Australia.
Hetényi, G., B. Taisne, F. Garel, É. Médard, S. Bosshard, and H. B. Mattsson (2011), Scales of columnar jointing in igneous rocks: Field measurements and controlling factors, *Bull. Volcanol.*, *74*(2), 457–482, doi:10.1007/s00445-011-0534-4.
Hickman, S., R. Sibson, and R. Bruhn (1995), Introduction to special section: Mechanical involvement of fluids in faulting, *J. Geophys. Res.*, *100*(B7), 12,831–12,840, doi:10.1029/95JB01121.
Ishibashi, T., N. Watanabe, N. Hirano, A. Okamoto, and N. Tsuchiya (2014), Beyond-laboratory-scale prediction for channeling flows through subsurface rock fractures with heterogeneous aperture distributions revealed by laboratory evaluation, *J. Geophys. Res. Solid Earth*, *120*, 106–124, doi:10.1002/2014JB011555.
James, G., D. Witten, T. Hastie, and R. Tibshirani (2013), *An introduction to statistical learning*, Springer, New York, doi:10.1007/978-1-4614-7138-7.
Johnston, J. D., and K. J. W. McCaffrey (1996), Fractal geometries of vein systems and the variation of scaling relationships with mechanism, *J. Struct. Geol.*, *18*(2–3), 349–358, doi:10.1016/S0191-8141(96)80055-1.
Johri, M., E. M. Dunham, M. D. Zoback, and Z. Fang (2014), Predicting fault damage zones by modeling dynamic rupture propagation and comparison with field observations, *J. Geophys. Res. Solid Earth*, *119*, 1251–1272, doi:10.1002/2013jb010335.
Kissling, W. M., S. E. Ellis, D. D. McNamara, and C. Massiot (2015), Modelling fluid flow through fractured rock: Examples using TVZ geothermal reservoirs, paper presented at 37th New Zealand Geothermal Workshop, Taupo, New Zealand, 18-20 Nov.
Kulander, B. R., S. L. Dean, and B. J. Ward (1990), Fractured core analysis: Interpretation, logging, and use of natural and induced fractures in core, in *AAPG Methods in Exploration Series 8*, AAPG, Tulsa, Okla., 88 pp.
Lachassagne, P., B. Aunay, N. Frissant, M. Guilbert, and A. Malard (2014), High-resolution conceptual hydrogeological model of complex basaltic volcanic islands: A Mayotte, Comoros, case study, *Terra Nova*, *26*(4), 307–321, doi:10.1111/ter.12102.
Ladeira, F., and N. Price (1981), Relationship between fracture spacing and bed thickness, *J. Struct. Geol.*, *3*(2), 179–183, doi:10.1016/0191-8141(81)90013-4.
Limpert, E., W. A. Stahel, and M. Abbt (2001), Log-normal distributions across the sciences: Keys and clues, *BioScience*, *51*(5), 341–352, doi:10.1641/0006-3568(2001)051[0341:lndats]2.0.co;2.
Litchfield, N., et al. (2014), A model of active faulting in New Zealand, *N. Z. J. Geol. Geophys.*, *57*(1), 32–56, doi:10.1080/00288306.2013.854256.
Manzocchi, T., C. Childs, and J. J. Walsh (2010), Faults and fault properties in hydrocarbon flow models, *Geofluids*, *10*(1–2), 94–113, doi:10.1111/j.1468-8123.2010.00283.x.

Massiot, C., G. Bignall, S. Alcaraz, A. J. Rae, F. Sepulveda, and H. van Moerkerk (2011), Testing the effectiveness of Leapfrog geothermal 3-D integrated geological modelling as a geothermal resource exploration and management tool, *Geotherm. Resour. Coucil Trans.*, *35*, 905–909.

Massiot, C., D. McNamara, and B. Lewis (2015), Processing and analysis of high temperature geothermal acoustic borehole image logs in the Taupo Volcanic Zone, New Zealand, *Geothermics*, *53*, 190–201, doi:10.1016/j.geothermics.2014.05.010.

Massiot, C., J. Townend, A. Nicol, and D. D. McNamara (2017a), Statistical methods of fracture characterisation based on acoustic borehole televiewer log analysis, *J. Geophys. Res. Solid Earth*, *122*, doi:10.1002/2017JB014115.

Massiot, C., A. Nicol, J. Townend, D. D. McNamara, D. Garcia-Selles, C. E. Conway, and G. C. Archibald (2017b), Quantitative geometric description of fracture systems in an andesite lava flow using terrestrial laser scanner data, *J. Volcanol. Geotherm. Res.*, *341*, 315–331, doi:10.1016/j.jvolgeores.2017.05.036.

Matter, J. M., et al. (2016), Rapid carbon mineralization for permanent disposal of anthropogenic carbon dioxide emissions, *Science*, *352*(6291), 1312–1314, doi:10.1126/science.aad8132.

McCaffrey, K. J. W., J. M. Sleight, S. Pugliese, and R. E. Holdsworth (2003), Fracture formation and evolution in crystalline rocks: Insights from attribute analysis, *Geol. Soc. London Spec. Publ.*, *214*(1), 109–124, doi:10.1144/gsl.sp.2003.214.01.07.

McNamara, D. D., and C. Massiot (2016), Geothermal Structural Geology in New Zealand: innovative characterisation and micro-analytical techniques, paper presented at 38th New Zealand Geothermal Workshop, Auckland, New Zealand, 23-25 Nov.

McNamara, D. D., C. Massiot, B. Lewis, and I. C. Wallis (2015), Heterogeneity of structure and stress in the Rotokawa Geothermal Field, New Zealand, *J. Geophys. Res. Solid Earth*, *120*, 1243–1262, doi:10.1002/2014JB011480.

McNamara, D. D., S. Sewell, E. Buscarlet, and I. C. Wallis (2016a), A review of the Rotokawa Geothermal Field, New Zealand, *Geothermics*, *59*(B), 281–293, doi:10.1016/j.geothermics.2015.07.007.

McNamara, D. D., A. Lister, and D. J. Prior (2016b), Calcite sealing in a fractured geothermal reservoir: Insights from combined EBSD and chemistry mapping, *J. Volcanol. Geotherm. Res.*, *323*, 38–52, doi:10.1016/j.jvolgeores.2016.04.042.

Milloy, S. F., and Y. W. Lim (2012), Wairakei-Tauhara pressure regime update, paper presented at the New Zealand Geothermal Workshop, Auckland, New Zealand, 19-21 Nov.

Misra, S., S. Ellis, and N. Mandal (2015), Fault damage zones in mechanically layered rocks: The effects of planar anisotropy, *J. Geophys. Res. Solid Earth*, *120*, 5432–5452, doi:10.1002/2014JB011780.

Mroczek, E. K., S. D. Milicich, P. F. Bixley, F. Sepulveda, E. A. Bertrand, S. Soengkono, and A. J. Rae (2016), Ohaaki geothermal system: Refinement of a conceptual reservoir model, *Geothermics*, *59*(B), 311–324, doi:10.1016/j.geothermics.2015.09.002.

Nemčok, M., J. N. Moore, R. Allis, and J. McCulloch (2004), Fracture development within a stratovolcano: The Karaha-Telaga Bodas geothermal field, Java volcanic arc, *Geol. Soc. London Spec. Publ.*, *231*(1), 223–242, doi:10.1144/gsl.sp.2004.231.01.13.

Nemčok, M., J. N. Moore, C. Christensen, R. Allis, T. Powell, B. Murray, and G. Nash (2007), Controls on the Karaha-Telaga Bodas geothermal reservoir, Indonesia, *Geothermics*, *36*(1), 9–46, doi:10.1016/j.geothermics.2006.09.005.

Nicol, A., J. Walsh, J. Watterson, and P. Gillespie (1996), Fault size distributions—Are they really power-law?, *J. Struct. Geol.*, *18*(2–3), 191–197, doi:10.1016/s0191-8141(96)80044-7.

Nicol, A., J. Walsh, K. Berryman, and P. Villamor (2006), Interdependence of fault displacement rates and paleoearthquakes in an active rift, *Geology*, *34*(10), 865–868, doi:10.1130/g22335.1.

Özkaya, S. I. (2003), Fracture length estimation from borehole image logs, *Math. Geol.*, *35*(6), 737–753, doi:10.1023/b:matg.0000002987.69549.ba.

Pérez-Flores, P., E. Veloso, J. Cembrano, P. Sánchez-Alfaro, M. Lizama, and G. Arancibia (2017), Fracture network, fluid pathways and paleostress at the Tolhuaca geothermal field, *J. Struct. Geol.*, *96*, 134–148, doi:10.1016/j.jsg.2017.01.009.

Pickering, G., J. Bull, and D. Sanderson (1995), Sampling power-law distributions, *Tectonophysics*, *248*(1–2), 1–20, doi:10.1016/0040-1951(95)00030-q.

Place, J., J. Sausse, J.-M. Marthelot, M. Diraison, Y. Géraud, and C. Naville (2011), 3-D mapping of permeable structures affecting a deep granite basement using isotropic 3C VSP data, *Geophys. J. Int.*, *186*(1), 245–263, doi:10.1111/j.1365-246x.2011.05012.x.

Pollyea, R. M., J. P. Fairley, R. K. Podgorney, and T. L. Mcling (2014), Physical constraints on geologic CO_2 sequestration in low-volume basalt formations, *Geol. Soc. Am. Bull.*, *126*(3–4), 344–351, doi:10.1130/b30874.1.

Priest, S. D. (1993), *Discontinuity Analysis for Rock Engineering*, Springer, Netherlands, doi:10.1007/978-94-011-1498-1.

Radilla, G., J. Sausse, B. Sanjuan, and M. Fourar (2012), Interpreting tracer tests in the Enhanced Geothermal System (EGS) of Soultz-sous-Forêts using the equivalent stratified medium approach, *Geothermics*, *44*, 43–51, doi:10.1016/j.geothermics.2012.07.001.

Rae, A. J., (2007), Rotokawa geology and geophysics, Tech. Rep., GNS Science Consultancy Rep. 2007/83, Taupo, New Zealand.

Rae, A. J., A. McCoy-West, L. Ramirez, and D. D. McNamara, (2010), Geology of production wells RK30L1 and RK30L2, Rotokawa geothermal field, Tech. Rep., GNS Science Consultancy Rep. 2010/02, Taupo, New Zealand.

Ramirez, L. E., and A. J. Rae, (2009), Geology of injection well RK24/RK24 ST1 Rotokawa geothermal field, Tech. Rep., GNS Science Consultancy Rep. 2009/90, Taupo, New Zealand.

Reynolds, A. P., G. Richards, B. de la Iglesia, and V. J. Rayward-Smith (2006), Clustering rules: A comparison of partitioning and hierarchical clustering algorithms, *J. Math. Model. Algo.*, *5*(4), 475–504, doi:10.1007/s10852-005-9022-1.

Risk, G. F. (2000), Electrical resistivity surveys of the Rotokawa Geothermal Field, New Zealand, paper presented at the 22nd New Zealand Geothermal Workshop, pp. 121–126, Geothermal Workshop, Univ. of Auckland, New Zealand.

Rives, T., M. Razack, J.-P. Petit, and K. Rawnsley (1992), Joint spacing: Analogue and numerical simulations, *J. Struct. Geol.*, *14*(8–9), 925–937, doi:10.1016/0191-8141(92)90024-q.

Rowland, J. V., and R. H. Sibson (2001), Extensional fault kinematics within the Taupo Volcanic Zone, New Zealand: Soft-linked segmentation of a continental rift system, *N. Z. J. Geol. Geophys.*, *44*(2), 271–283, doi:10.1080/00288306.2001.9514938.

Rowland, J. V., and S. F. Simmons (2012), Hydrologic, magmatic, and tectonic controls on hydrothermal flow, Taupo Volcanic Zone, New Zealand: Implications for the formation of epithermal vein deposits, *Econ. Geol.*, *107*(3), 427–457, doi:10.2113/econgeo.107.3.427.

Rowland, J. V., C. J. Wilson, and D. M. Gravley (2010), Spatial and temporal variations in magma-assisted rifting, Taupo Volcanic Zone, New Zealand, *J. Volcanol. Geotherm. Res.*, *190*(1–2), 89–108, doi:10.1016/j.jvolgeores.2009.05.004.

Sasaki, M. (2006), Statistical features of vein systems in the Hishikari epithermal gold deposit, Japan, *Resour. Geol.*, *56*(1), 27–36, doi:10.1111/j.1751-3928.2006.tb00265.x.

Schöpfer, M. P., A. Arslan, J. J. Walsh, and C. Childs (2011), Reconciliation of contrasting theories for fracture spacing in layered rocks, *J. Struct. Geol.*, *33*(4), 551–565, doi:10.1016/j.jsg.2011.01.008.

Seebeck, H., A. Nicol, T. Stern, H. Bibby, and V. Stagpoole (2010), Fault controls on the geometry and location of the Okataina Caldera, Taupo Volcanic Zone, New Zealand, *J. Volcanol. Geotherm. Res.*, *190*(1–2), 136–151, doi:10.1016/j.jvolgeores.2009.04.011.

Seebeck, H., A. Nicol, P. Villamor, J. Ristau, and J. Pettinga (2014a), Structure and kinematics of the Taupo Rift, New Zealand, *Tectonics*, *33*(6), 1178–1199, doi:10.1002/2014TC003569.

Seebeck, H., A. Nicol, J. Walsh, C. Childs, R. Beetham, and J. Pettinga (2014b), Fluid flow in fault zones from an active rift, *J. Struct. Geol.*, *62*, 52–64, doi:10.1016/j.jsg.2014.01.008.

Sherburn, S., S. Sewell, S. Bourguignon, W. Cumming, S. Bannister, C. Bardsley, J. Winick, J. Quinao, and I. Wallis (2015), Microseismicity at Rotokawa geothermal field, New Zealand, 2008–2012, *Geothermics*, *54*, 23–34, doi:10.1016/j.geothermics.2014.11.001.

Simpson, M. P., S. S. Palinkas, M. Nieuwoudt, R. J. Bodnar, and J. L. Mauk (2015), Geothermal systems and epithermal deposits of New Zealand: A fluid chemistry comparison, paper presented at the 37th New Zealand Geothermal Workshop, Taupo, New Zealand, 18-20 Nov.

Siratovich, P. A., M. J. Heap, M. C. Villeneuve, J. W. Cole, and T. Reuschlé (2014), Physical property relationships of the Rotokawa Andesite, a significant geothermal reservoir rock in the Taupo Volcanic Zone, New Zealand, *Geotherm. Energy*, *2*, 10, doi:10.1186/s40517-014-0010-4.

Siratovich, P. A., M. J. Heap, M. C. Villeneuve, J. W. Cole, B. M. Kennedy, J. Davidson, and T. Reuschlé (2016), Mechanical behaviour of the Rotokawa Andesites (New Zealand): Insight into permeability evolution and stress-induced behaviour in an actively utilised geothermal reservoir, *Geothermics*, *64*, 163–179, doi:10.1016/j.geothermics.2016.05.005.

Spörli, K. B., and H. Cargill (2011), Structural evolution of a world-class epithermal orebody: The Martha Hill deposit, Waihi, New Zealand, *Econ. Geol.*, *106*(6), 975–998, doi:10.2113/econgeo.106.6.975.

Stasinopoulos, D. M., and R. A. Rigby (2007), Generalized Additive Models for Location Scale and Shape (GAMLSS) in R, *J. Stat. Software*, *23*(7), 1–46, doi:10.18637/jss.v023.i07.

Terzaghi, R. D. (1965), Sources of error in joint surveys, *Géotechnique*, *15*(3), 287–304, doi:10.1680/geot.1965.15.3.287.

Townend, J., and M. D. Zoback (2000), How faulting keeps the crust strong, *Geology*, *28*(5), 399–402, doi:10.1130/0091-7613(2000)28<399:HFKTCS>2.0.CO;2.

Vermilye, J. M., and C. H. Scholz (1995), Relation between vein length and aperture, *J. Struct. Geol.*, *17*(3), 423–434, doi:10.1016/0191-8141(94)00058-8.

Villamor, P., and K. R. Berryman (2001), A Late Quaternary extension rate in the Taupo Volcanic Zone, New Zealand, derived from fault slip data, *N. Z. J. Geol. Geophys.*, *44*(2), 243–269, doi:10.1080/00288306.2001.9514937.

Villamor, P., and K. R. Berryman (2006), Evolution of the southern termination of the Taupo Rift, New Zealand, *N. Z. J. Geol. Geophys.*, *49*(1), 23–37, doi:10.1080/00288306.2006.9515145.

Wallace, L. M., J. Beavan, R. McCaffrey, and D. Darby (2004), Subduction zone coupling and tectonic block rotations in the North Island, New Zealand, *J. Geophys. Res.*, *109*, doi:10.1029/2004JB003241.

Wallis, I. C., C. Bardsley, T. Powell, J. V. Rowland, and J. M. O'Brien (2013), A structural model for the Rotokawa Geothermal Field, New Zealand, paper presented at the New Zealand Geothermal Workshop, Rotorua, New Zealand, 17–20 Nov.

Wang, X. (2005), Stereological interpretation of rock fracture traces on borehole walls and other cylindrical surfaces, PhD thesis, Virginia Polytech. Inst. and State Univ., Blacksburg, Va.

Wilson, C., B. Houghton, M. McWilliams, M. Lanphere, S. Weaver, and R. Briggs (1995), Volcanic and structural evolution of Taupo Volcanic Zone, New Zealand: A review, *J. Volcanol. Geotherm. Res.*, *68*(1–3), 1–28, doi:10.1016/0377-0273(95)00006-g.

Wilson, C. J. N., and J. V. Rowland (2016), The volcanic, magmatic and tectonic setting of the Taupo Volcanic Zone, New Zealand, reviewed from a geothermal perspective, *Geothermics*, *59*(B), 168–187, doi:10.1016/j.geothermics.2015.06.013.

Wyering, L. D., M. C. Villeneuve, I. C. Wallis, P. A. Siratovich, B. M. Kennedy, D. Gravley, and J. L. Cant (2014), Mechanical and physical properties of hydrothermally altered rocks, Taupo Volcanic Zone, New Zealand, *J. Volcanol. Geotherm. Res.*, *288*, 76–93, doi:10.1016/j.jvolgeores.2014.10.008.

Zuquim, M., and J. V. Rowland (2013), Structural controls on fluid flow at the Onemana area, Coromandel Peninsula, New Zealand, paper presented at the 35th NZ Geothermal Workshop, Rotorua, New Zealand, 17–20 Nov.